

Learning Scene-Level Signed Directional Distance Function with Ellipsoidal Priors and Neural Residuals

Zhirui Dai Hojoon Shin Yulun Tian Ki Myung Brian Lee Nikolay Atanasov

Department of Electrical and Computer Engineering

University of California, San Diego

La Jolla, CA 92093 USA

Email: {zh dai, hoshin, kmblee, yut034, natanasov}@ucsd.edu

Abstract—Dense geometric environment representations are critical for autonomous mobile robot navigation and exploration. Recent work shows that implicit continuous representations of occupancy, signed distance, or radiance learned using neural networks offer advantages in reconstruction fidelity, efficiency, and differentiability over explicit discrete representations based on meshes, point clouds, and voxels. In this work, we explore a directional formulation of signed distance, called signed directional distance function (SDDF). Unlike signed distance function (SDF) and similar to neural radiance fields (NeRF), SDDF has a position and viewing direction as input. Like SDF and unlike NeRF, SDDF directly provides distance to the observed surface along the direction, rather than integrating along the view ray, allowing efficient view synthesis. To learn and predict scene-level SDDF efficiently, we develop a differentiable hybrid representation that combines explicit ellipsoid priors and implicit neural residuals. This approach allows the model to effectively handle large distance discontinuities around obstacle boundaries while preserving the ability for dense high-fidelity prediction. We show that SDDF is competitive with the state-of-the-art neural implicit scene models in terms of reconstruction accuracy and rendering efficiency, while allowing differentiable view prediction for robot trajectory optimization.

I. INTRODUCTION

Robots are increasingly deployed and expected to operate autonomously in a priori unknown and unstructured environments. This requires efficient representation and prediction of environment geometry from sensor observations, e.g., depth images or LiDAR scans, to support collision checking for safe navigation, occlusion prediction for autonomous exploration, or grasp pose generation for object manipulation. While many explicit environment representations, based on meshes [28, 33], point clouds [5, 34], and voxels [13], can be constructed from sensor measurements and have been used successfully, their occupancy estimation is not continuous and does not support differentiation. The former hurts the reconstruction accuracy, while the latter makes collision checking and novel view synthesis operations inefficient.

Recent work has focused on implicit scene representations that support differentiable geometry reconstruction and novel view synthesis. For example, occupancy networks [24] and DeepSDF [29] have shown impressive results by representing surfaces as the zero level set of an occupancy probability function or a signed distance function (SDF). Neural radiance field (NeRF) [25] and Gaussian splatting (GS) [18] models learn geometry implicitly through 2D image rendering supervision.

Although these implicit differentiable methods offer superior fidelity, they require multiple network forward passes, complicated calculations per pixel/ray, and high memory usage.

A promising recent approach that overcomes these limitations is the signed directional distance function (SDDF). SDDF is a directional formulation of SDF that takes a position and a viewing direction as input (like NeRF and unlike SDF) and provides the distance to the observed surface along the viewing direction (like SDF and unlike NeRF, which integrates radiance along the view ray). The benefits of estimating SDDF are three-fold. First, SDDF models can provide fast, single forward-pass directional distance queries in a differentiable way, supporting operations such as novel view synthesis and differentiable view optimization. Second, SDDF models can be trained from different kinds of sensor data, including depth images and LiDAR scans, as long as they can be converted to ray distances. This is in contrast with SDF models, which require processing of sensor measurements to obtain SDF supervision data, and with NeRF and GS models that commonly expect camera images. Third, an SDDF model learns a geometry representation in the space of positions and directions, which allows arbitrary view synthesis and efficient occlusion queries. This is in contrast with an SDF model which requires an iterative sphere tracing algorithm [11] to compute distance in a desired direction.

However, learning scene-level geometry in the space of positions and directions is challenging. In comparison to SDF, introducing direction as an additional input requires additional training data with diverse viewing directions to provide sufficient supervision. Another difficulty is that SDDF is sensitive to the ray positions and directions because occlusions introduce discontinuities in the observed distance. For these reasons, previous methods closest to ours for learning directional distance models [50, 3] are only applicable to single object shape modeling. In contrast, we consider learning scene-level SDDFs, which is necessary for robot navigation but exacerbates the aforementioned challenges.

To address these challenges, we propose a method that combines the advantages of explicit and implicit representations to learn SDDF at the scene level. As shown in Fig. 1, our method first constructs an explicit ellipsoid-based prior to capture the coarse structure and occlusions of the environment. Then, an implicit residual neural network model corrects the

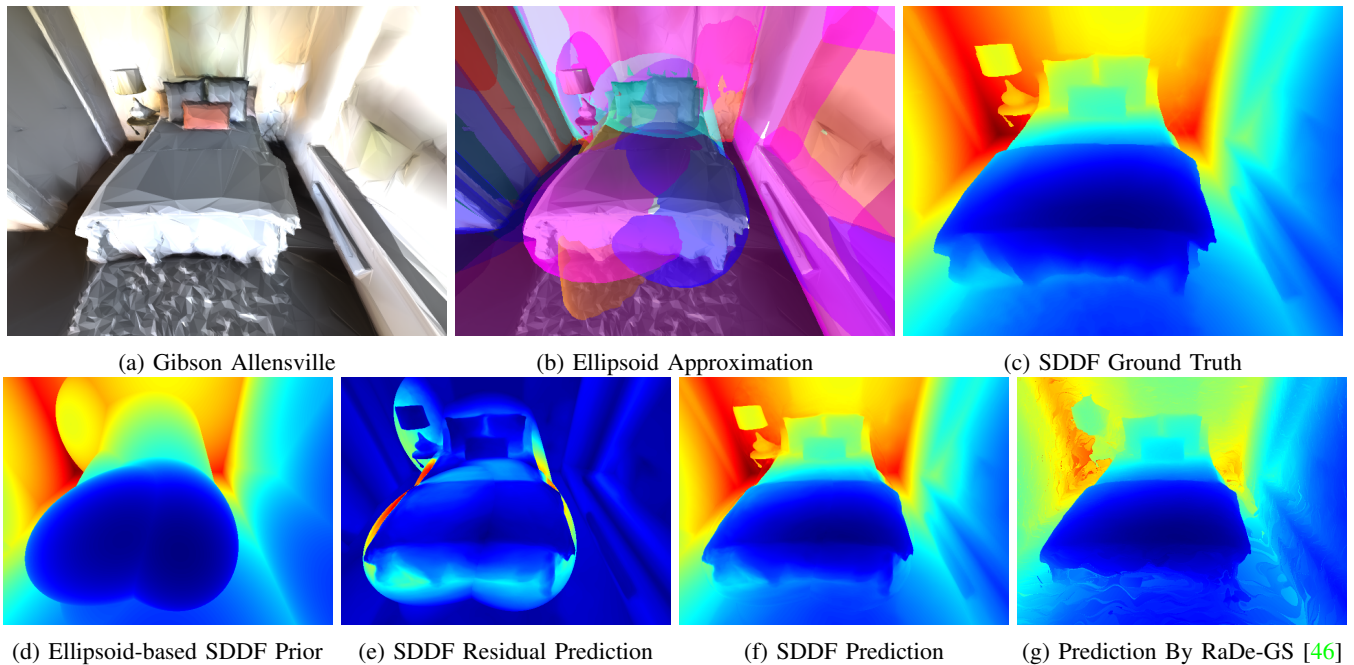


Fig. 1: (a), (c): We present a method to learn scene-level signed directional distance function (SDDF). (a), (b), (d): Our method uses ellipsoids as an initial coarse approximation of the shapes of objects in the environment. (e), (f): The ellipsoid prior is refined by a latent feature network and a shared decoder to predict the surface reconstruction residual. (f), (g): Our SDDF learning method offers single-query differentiable novel distance image synthesis without RGB supervision as an alternative to Gaussian Splat distance rendering (e.g., RaDe-GS [46]) or signed distance function sphere tracing (e.g., InstantNGP [26]).

coarse ellipsoid predictions with precise details that capture the fine structure of the environment. We guarantee that both the ellipsoid prior and the residual network are differentiable and, hence, our SDDF model supports single-query novel view synthesis and differentiable view optimization. In summary, this paper makes the following contributions.

- We define a signed directional distance function suitable for scene-level representation.
- We design a hybrid explicit-implicit model to approximate SDDF, consisting of an ellipsoid-based prior and an implicit neural residual, and guarantee that SDDF predictions of our complete model satisfy an Eikonal distance constraint by construction.
- We develop an algorithm to initialize the ellipsoid prior and derive the gradients with respect to its parameters in closed-form to accelerate training.
- Our experiments show that our method is competitive with state-of-the-art SDF, GS, and NeRF in Replica and Gibson scene reconstruction in terms of reconstruction accuracy, rendering speed, and GPU memory cost.

II. RELATED WORK

Three bodies of work are related to ours, which are NeRFs, implicit geometric representations, and directional distance functions (DDFs).

A. Neural Radiance Fields

Radiance field is a promising recent direction in scene representation that has led to a significant improvement in the syn-

thesis of novel photometric views. The original NeRF [25, 38] employed volumetric rendering with a neural network trained to predict the color and opacity along a view direction at a given position, which are then integrated for rendering. Such volumetric rendering, however, is computationally expensive because many samples are required for integration. To mitigate this, subsequent approaches [47, 4, 9, 12] introduce explicit data structures for faster and more accurate rendering with a smaller memory footprint. For example, PlenOctree [45] and Plenoxel [8] use voxelized data structures such as an octree [45] or a regular grid [8] to store SH coefficients for better efficiency. Similarly, neural point methods [1, 31, 43, 48] use point clouds to store SH coefficients or neural features. Gaussian splatting (GS) [18] and its variants such as 2D-GS [15] and rasterizing depth GS (RaDe-GS) [46] explore this direction further by using a large number of Gaussians with SH coefficients that can be explicitly rasterized to an image through a projective transform. These methods show that a hybrid model combining an explicit representation (e.g., point cloud, octree, or Gaussians) with an implicit representation (e.g., SH coefficients, or neural features) can offer a better trade-off between rendering quality and speed. Drawing inspiration from these methods, we also design a hybrid explicit-implicit scene representation. However, we focus on geometric accuracy instead of photometric accuracy.

B. Implicit Geometric Representations

Many previous scene representations also focus on geometric accuracy as we do. Distance representations such as signed

distance function (SDF), unsigned distance function (UDF) [23], and truncated SDF (TSDF) [27], are especially popular in robotics because they offer fast proximity queries for collision checking [20], and are often differentiable for trajectory optimization [41, 51]. Voxelblox [28] uses voxel hashing to incrementally estimate and store SDF in a hierarchical voxel data structure. Gaussian process (GP) methods [19, 40] use octrees to store incrementally estimated oriented surface points and the corresponding GP models to regress SDF. Although these methods achieve real-time incremental SDF estimation, they fail to capture small-scale details accurately.

Recent approaches such as DeepSDF [29] and implicit geometric regularization (IGR) [10] demonstrate that neural networks can learn SDF accurately, with supervision from oriented surface points and Eikonal regularization [10]. To learn a geometric representation from images instead of surface points, geometric representations can be incorporated in a radiance field and used as a means to improve photometric accuracy. For example, NeuS [39] replaces the opacity with an SDF so that the geometry (i.e. SDF) and the radiance field are learned together. For RaDe-GS, Zhang et al. [46] propose a geometric regularization term that improves both geometric and photometric accuracy. These results show that an accurate geometric representation that we pursue here is fundamentally important for both geometric and photometric accuracy.

For geometric supervision, SDFDiff [16] and DIST [21] use depth, surface normals, or silhouette for supervision by differentiating through SDF queries in sphere tracing iterations, although the sphere tracing process [11] itself is not differentiable. Sphere tracing on SDFs can also be used to compute directional distance as we do, but its iterative and cumulative nature leads to not only slower training and rendering, but also error accumulation.

C. Directional Distance Functions

Instead, DDFs provide directional distance in a single query, and are hence more efficient and free from error accumulation. Directional TSDF [35] extends TSDF in 3D to six voxel grids, each along or against the X , Y , and Z axes. This is not a directional distance field, but rather six independent voxel grids of TSDF estimated along different axis directions. Despite limited surface reconstruction accuracy due to voxelization, the method shows the importance of directional information when modeling thin objects. More relevant is the signed ray distance function (SRDF) [49], which is defined with respect to a given camera pose, as the distance of a 3D point to the scene surface along the viewing lines of the camera. This definition is useful for multiview stereo because SRDF is zero only when the query point is on the surface. Volrecon [32] uses the same term, SRDF, to instead denote simply the distance between a point and the scene surface along a ray, which is closer to our definition. This SRDF is used in volumetric rendering for multiview stereo and high-quality rendering, which shows the utility of the directional distance in capturing geometric details. However, Volrecon uses multiple transformers, and

many samples along each ray, which is prohibitively slow for scaling to larger scenes.

Except in multiview stereo applications, other previous methods focus on learning DDFs at the object level. NeuralODF [14] and RayDF [22] propose to learn ray-surface distances for an object bounded by a sphere that is used to parameterize the ray. Sphere-based ray parameterization cannot apply to scene-level DDF reconstruction because scenes may be unbounded. FIRE [44] combines SDF and DDF to reconstruct object shapes, where DDF renders object shapes efficiently. However, it is difficult to scale to scenes because FIRE requires silhouettes for good performance, which cannot be directly captured by sensors. Pointersect [6] uses a transformer to predict the ray travel distance, the surface normal vector, and RGB color given a dense point cloud generated from multiple posed RGB-D images. Due to the dense point cloud and the transformer, Pointersect exhibits slow rendering and lower output quality when multiple surfaces exist along the ray, which limits its scalability. The network architecture of Zobeidi and Atanasov [50] is smaller and more specialized for learning the SDDF of object shapes in that the Eikonal constraint is satisfied by construction. However, their definition and design are only suitable for learning a single object due to the omission of occlusions. The probabilistic DDF (PDDF) [3] handles more complex scenes by introducing an additional "probability" network to learn the discontinuities caused by occlusions and to combine multiple objects' DDFs into a scene. However, its scalability is limited since many independent networks are needed for each object in larger scenes. Moreover, the omission of sign information obfuscates whether a query position is inside or outside the objects. Instead, as shown in Fig. 2, our definition of SDDF has less discontinuities than DDF, and can encode complicated geometric structures ranging from small objects to large scenes.

III. METHOD OVERVIEW

We aim to design a method for mobile robots equipped with range sensors, such as LiDARs or depth cameras, to learn an environment model capable of efficient and differentiable synthesis of arbitrary distance views. Let the occupied space in the environment be represented by a set $\mathcal{O} \subset \mathbb{R}^n$, where n is the dimension ($n \in \{2, 3\}$ in practice). Consider a set of measurements $\{\mathbf{T}_t, \mathcal{Z}_t\}_{t=1}^T$, where $\mathbf{T}_t \in SE(n)$ is the sensor pose at time t and $\mathcal{Z}_t = \{\mathbf{v}_i, r_{t,i}\}_{i=1}^N$ are the measurements at time t , consisting of N viewing directions $\mathbf{v}_i \in \mathbb{S}^{n-1}$ (e.g., unit vector in the direction of each depth camera pixel or unit vector in the direction of each LiDAR scan ray) and corresponding range measurements $r_{t,i} \in \mathbb{R}_{>0}$. Our objective is to learn a representation of the occupied space \mathcal{O} in the form of a signed directional distance function.

Definition 1. The *signed directional distance function* (SDDF) of a set $\mathcal{O} \subset \mathbb{R}^n$ is a function $f : \mathbb{R}^n \times \mathbb{S}^{n-1} \rightarrow \mathbb{R} \cup \{\pm\infty\}$ that measures the signed distance from a point $\mathbf{p} \in \mathbb{R}^n$ to the

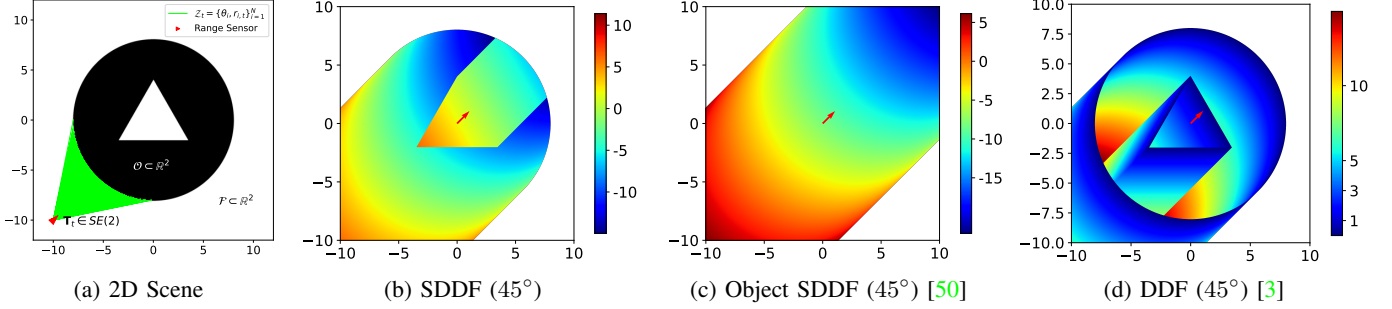


Fig. 2: Example of our scene-level SDDF, the object-level SDDF of [50], and the DDF of [3] in a 2D synthetic environment. A range sensor (red triangle) with pose $\mathbf{T}_t \in SE(2)$ is measuring the distance to a doughnut-like obstacle \mathcal{O} (black) with a triangular hole in the middle (left plot). At time t , the sensor measurement $\mathcal{Z}_t = \{\theta_i, r_{i,t}\}_{i=1}^N$ consists of N range measurements r_i obtained along rays (green lines) cast at angles θ_i . The red arrow in the three plots on the right labels the viewing direction. Unlike DDF, our SDDF definition is continuous when transitioning from free to occupied space along the viewing direction. Compared with object SDDF [50], our SDDF definition reflects the geometry well, allowing scene-level reconstruction.

set boundary $\partial\mathcal{O}$ along a direction $\mathbf{v} \in \mathbb{S}^{n-1}$, defined as:

$$f(\mathbf{p}, \mathbf{v}; \mathcal{O}) := \begin{cases} \min\{d > 0 \mid \mathbf{p} + d\mathbf{v} \in \partial\mathcal{O}\}, & \mathbf{p} \notin \mathcal{O}, \\ \max\{d \leq 0 \mid \mathbf{p} + d\mathbf{v} \in \partial\mathcal{O}\}, & \mathbf{p} \in \mathcal{O}. \end{cases} \quad (1)$$

The SDDF definition is illustrated in Fig. 2. For comparison, the signed distance function (SDF) of a set \mathcal{O} is defined as the shortest distance from $\mathbf{p} \in \mathbb{R}^n$ to the boundary $\partial\mathcal{O}$:

$$f_{\text{SDF}}(\mathbf{p}; \mathcal{O}) := \begin{cases} \min_{\mathbf{y} \in \partial\mathcal{O}} \|\mathbf{p} - \mathbf{y}\|_2, & \mathbf{p} \notin \mathcal{O}, \\ -\min_{\mathbf{y} \in \partial\mathcal{O}} \|\mathbf{p} - \mathbf{y}\|_2, & \mathbf{p} \in \mathcal{O}. \end{cases} \quad (2)$$

The SDF and SDDF of \mathcal{O} are related as follows:

$$f_{\text{SDF}}(\mathbf{p}; \mathcal{O}) = \min_{\mathbf{v} \in \mathbb{S}^{n-1}} f(\mathbf{p}, \mathbf{v}; \mathcal{O}). \quad (3)$$

It is well known [10, 40] that SDFs satisfy an Eikonal equation $\|\nabla_{\mathbf{p}} f_{\text{SDF}}(\mathbf{p}; \mathcal{O})\|_2 = 1$, which is useful for regularizing or designing the structure of models for estimating SDF. The next proposition shows that SDDF satisfies a similar property.

Proposition 1. *Suppose an SDDF $f(\mathbf{p}, \mathbf{v}; \mathcal{O})$ is differentiable at $\mathbf{p} \in \mathbb{R}^n$. Then, it satisfies a directional Eikonal equation:*

$$\mathbf{v}^\top \nabla_{\mathbf{p}} f(\mathbf{p}, \mathbf{v}; \mathcal{O}) = -1. \quad (4)$$

Proof: When the ray hits the same surface point $\mathbf{q} = \mathbf{p} + d\mathbf{v}$ as \mathbf{p} moves along \mathbf{v} , we have:

$$\begin{aligned} \mathbf{v}^\top \nabla_{\mathbf{p}} f(\mathbf{p}, \mathbf{v}; \mathcal{O}) &= \lim_{\delta \rightarrow 0} \frac{f(\mathbf{p} + \delta\mathbf{v}, \mathbf{v}) - f(\mathbf{p}, \mathbf{v})}{\delta} \\ &= \lim_{\delta \rightarrow 0} \frac{(d - \delta) - d}{\delta} = -1. \quad \blacksquare \end{aligned}$$

Previous work [50] proposes an object SDDF that is defined as $\min\{d \in \mathbb{R} \mid \mathbf{p} + d\mathbf{v} \in \partial\mathcal{O}\}$. However, this definition is only suitable for learning the shape of a single object because when there is another object behind the viewing position \mathbf{p} , the object SDDF will ignore the object that the viewing direction \mathbf{v} is pointing at. Fig. 2c shows an example of this issue.

PDDF [3] addresses this problem by learning directional distance without sign, defined as $\min\{d \geq 0 \mid \mathbf{p} + d\mathbf{v} \in$

$\partial\mathcal{O}\}$. However, as shown in Fig. 2d, this definition introduces several discontinuities, which is not favorable for learning a directional distance model from data.

Our definition of SDDF, shown in Fig. 2b, guarantees that the distance continuously changes from positive to negative values when a viewing ray \mathbf{v} enters the occupied space \mathcal{O} from *outside in*. However, when the ray leaves \mathcal{O} from *inside out*, there is a discontinuity in the distance. Fortunately, such discontinuity does not occur in practice because robotic sensors remain within free space, only observing \mathcal{O} from outside-in. Thus, our definition can accurately model occlusions, while retaining the sign to distinguish whether the query position is in free space, unlike previous formulations of DDF [3].

Yet, learning a solely continuous, implicit representation of our new SDDF definition remains challenging. Unlike an SDF, SDDF is sensitive to both position and direction as small input perturbations may lead to hitting a different obstacle surface, resulting in a significant change in SDDF value. The inherent discontinuity and the added input dimensions for the ray direction demand more training data over different ray directions. Explicit representations have advantages in handling such discontinuities with less data, but purely explicit representations struggle to achieve high-fidelity reconstruction and differentiable view synthesis as they are discrete. In contrast, implicit representations are good at learning geometric details and allow differentiation.

Therefore, as shown in Fig. 3, our model combines both explicit and implicit representations. First, in Sec. IV, an explicit ellipsoid-based Prior network $P(\mathbf{p}, \mathbf{v})$ is introduced to predict a coarse SDDF prior $f(\mathbf{p}, \mathbf{v})$. Then, in Sec. V, we present a residual network consisting of a Latent feature network L and a Residual decoder R that predicts an SDDF correction $\delta_f(\mathbf{p}, \mathbf{v})$, so that the combination accurately models the true SDDF $f^*(\mathbf{p}, \mathbf{v})$ as $\hat{f}(\mathbf{p}, \mathbf{v}) = f(\mathbf{p}, \mathbf{v}) + \delta_f(\mathbf{p}, \mathbf{v})$.

IV. ELLIPSOID-BASED PRIOR NETWORK

To take advantage of an explicit representation for occlusion modeling, we design an ellipsoid-based prior network P . The

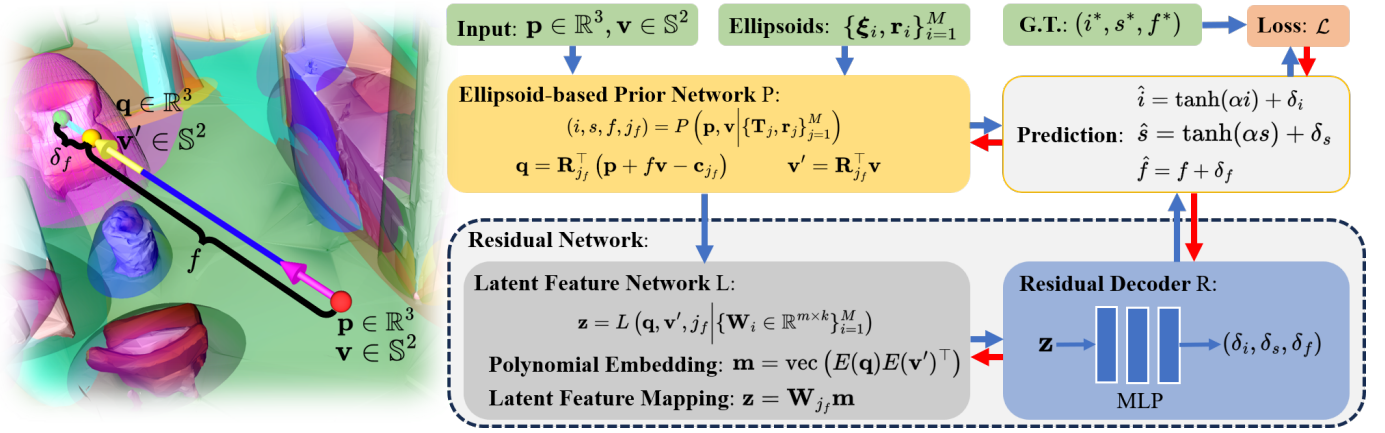


Fig. 3: **Method overview.** Given a query ray from position $\mathbf{p} \in \mathbb{R}^3$ in direction $\mathbf{v} \in \mathbb{S}^2$, an ellipsoid-based Prior network P uses M ellipsoids $\{\xi_i, \mathbf{r}_i\}_{i=1}^M$ to learn the rough shape of the environment such that it can determine the closest ellipsoid intersected by the ray and predict an SDDF prior. Then, with the intersection point $\mathbf{q} \in \mathbb{R}^3$ and ray direction $\mathbf{v}' \in \mathbb{S}^2$ in the ellipsoid’s local frame, a Latent network L generates a latent feature $\mathbf{z} \in \mathbb{R}^m$, which is decoded by the Residual decoder R into residual predictions $(\delta_i, \delta_s, \delta_f)$, i.e. the difference between the ground truth and the prior. Finally, we compose the SDDF prediction as $\hat{f} = f + \delta_f$. Blue arrows show the data flow in the forward pass, while red arrows represent the backward pass.

prior uses a set of ellipsoids to approximate the structure of the environment based on the range measurements and leaves the task of learning fine details to the residual network R .

A. SDDF of a Single Ellipsoid

First, for simplicity, consider a single ellipsoid given by:

$$\mathcal{E} = \{\mathbf{y} \in \mathbb{R}^3 \mid (\mathbf{y} - \mathbf{c})^\top \mathbf{R} \mathbf{Q}_0^{-2} \mathbf{R}^\top (\mathbf{y} - \mathbf{c}) \leq 1\}, \quad (5)$$

where $\mathbf{c} \in \mathbb{R}^3$ and $\mathbf{R} \in SO(3)$ are the position and orientation, $\mathbf{Q}_0 = \text{diag}(\mathbf{r})$, and $\mathbf{r} \in \mathbb{R}_+^3$ are the radii of the ellipsoid.

We parameterize the ellipsoid pose as:

$$\mathbf{T} = \begin{bmatrix} \mathbf{R} & \mathbf{c} \\ \mathbf{0}^\top & 1 \end{bmatrix} = \mathbf{T}_0 \exp(\xi^\wedge), \quad \xi^\wedge = \begin{bmatrix} \theta^\wedge & \rho \\ \mathbf{0}^\top & 0 \end{bmatrix}, \quad (6)$$

where $\mathbf{T}_0 \in SE(3)$ is initialized and fixed and $\xi = (\rho, \theta) \in \mathbb{R}^6$ is learnable. In (6), the function θ^\wedge maps a vector $\theta \in \mathbb{R}^3$ to a corresponding skew-symmetric matrix and \exp is the matrix exponential function.

To ensure that the radii $\mathbf{r} \in \mathbb{R}_+^3$, we parameterize it as $\mathbf{r} = \mathbf{r}_0 \exp(\mathbf{s})$, where $\mathbf{r}_0 \in \mathbb{R}_+^3$ is initialized and fixed, $\mathbf{s} \in \mathbb{R}^3$ is learnable, and \exp is applied element-wise.

Then, we derive the SDDF of an ellipsoid \mathcal{E} in closed form.

Proposition 2. Consider a ray from position $\mathbf{p} \in \mathbb{R}^3$ in direction $\mathbf{v} \in \mathbb{S}^2$ and ellipsoid $\mathcal{E} \subset \mathbb{R}^3$. If the ray does not intersect \mathcal{E} , the ellipsoid SDDF is $f(\mathbf{p}, \mathbf{v}; \mathcal{E}) = \infty$. Otherwise:

$$f(\mathbf{p}, \mathbf{v}; \mathcal{E}) = -\frac{\det \mathbf{Q}_0 \sqrt{i(\mathbf{p}, \mathbf{v})} + \mathbf{p}'^\top \mathbf{Q}_1^2 \mathbf{v}'}{\mathbf{v}'^\top \mathbf{Q}_1^2 \mathbf{v}'}, \quad (7)$$

where

$$i(\mathbf{p}, \mathbf{v}) = \mathbf{v}'^\top \mathbf{Q}_1^2 \mathbf{v}' - \mathbf{w}'^\top \mathbf{Q}_0^2 \mathbf{w}' \quad (8)$$

is an intersection indicator; $\mathbf{Q}_1 = \det(\mathbf{Q}_0) \mathbf{Q}_0^{-1}$, $\mathbf{p}' = \mathbf{R}^\top (\mathbf{p} - \mathbf{c})$, $\mathbf{v}' = \mathbf{R}^\top \mathbf{v}$, and $\mathbf{w}' = \mathbf{p}' \times \mathbf{v}'$.

Proof: Please refer to Appendix. A-A. ■

The intersection indicator $i(\mathbf{p}, \mathbf{v})$ in (8) is positive when the line through \mathbf{p} in direction \mathbf{v} intersects \mathcal{E} and negative otherwise. When the line is tangent to the ellipsoid, we have $i(\mathbf{p}, \mathbf{v}) = 0$. We also introduce a sign indicator:

$$s(\mathbf{p}, \mathbf{v}) = \mathbf{p}'^\top \mathbf{Q}_1^2 \mathbf{p}' - \det \mathbf{Q}_0^2, \quad (9)$$

which is negative when $\mathbf{p} \in \mathcal{E}$ and positive otherwise. We use the above equation instead of $\mathbf{p}'^\top \mathbf{Q}_0^{-2} \mathbf{p}' - 1$ as the sign indicator for better numerical stability.

In order to specify a reasonable SDDF prior when the line does not intersect the ellipsoid, i.e., when $i(\mathbf{p}, \mathbf{v}) < 0$, we change the SDDF from ∞ to:

$$f(\mathbf{p}, \mathbf{v}; \mathcal{E}) = -\frac{\mathbf{p}'^\top \mathbf{Q}_1^2 \mathbf{v}'}{\mathbf{v}'^\top \mathbf{Q}_1^2 \mathbf{v}'}. \quad (10)$$

The expression in (10) gives the distance from \mathbf{p}' along \mathbf{v}' to a virtual plane at the ellipsoid origin with normal vector $\mathbf{Q}_1^2 \mathbf{v}' / \|\mathbf{Q}_1^2 \mathbf{v}'\|_2$. This guarantees that $f(\mathbf{p}, \mathbf{v}; \mathcal{E})$ changes smoothly when $i(\mathbf{p}, \mathbf{v})$ changes sign.

The expression in (7) is valid only when the ray from \mathbf{p} in the direction of \mathbf{v} intersects \mathcal{E} . If the ellipsoid \mathcal{E} is behind the ray, i.e., $\mathbf{p} \notin \mathcal{E}$ and $s(\mathbf{p}, \mathbf{v}) > 0$, then (7) is negative but $f(\mathbf{p}, \mathbf{v}; \mathcal{E}) = \infty$. We introduce a validity function $v(\mathbf{p}, \mathbf{v})$, which is negative when \mathcal{E} is behind the view ray. This allows us to combine (7) and (10) with consideration of validity to obtain a modified SDDF prior for a single ellipsoid:

$$f(\mathbf{p}, \mathbf{v}; \mathcal{E}) = \begin{cases} -\frac{\det \mathbf{Q}_0 \sqrt{\beta} + \mathbf{p}'^\top \mathbf{Q}_1^2 \mathbf{v}'}{\mathbf{v}'^\top \mathbf{Q}_1^2 \mathbf{v}'}, & v(\mathbf{p}, \mathbf{v}) \geq 0, \\ \infty, & v(\mathbf{p}, \mathbf{v}) < 0, \end{cases} \quad (11)$$

where $\beta = \max(i(\mathbf{p}, \mathbf{v}), 0) + \epsilon$, $\epsilon > 0$ is a small value introduced for numerical stability of backward propagation, and the validity indicator function is defined as:

$$v(\mathbf{p}, \mathbf{v}) = -\frac{\det \mathbf{Q}_0 \sqrt{\beta} + \mathbf{p}'^\top \mathbf{Q}_1^2 \mathbf{v}'}{\mathbf{v}'^\top \mathbf{Q}_1^2 \mathbf{v}'} s(\mathbf{p}, \mathbf{v}). \quad (12)$$

A 2D example in Fig. 4 shows that the ellipsoid SDDF prior $f(\mathbf{p}, \mathbf{v}; \mathcal{E})$ in (11) reflects Definition. 1 correctly.

B. Fusing Multiple Ellipsoid SDDFs

To model scenes with multiple objects at different locations, we consider a set of M ellipsoids \mathcal{E}_j for $1 \leq j \leq M$. Sec. IV-A showed how to determine the SDDF $f_j(\mathbf{p}, \mathbf{v})$, intersection indicator $i_j(\mathbf{p}, \mathbf{v})$, and sign indicator $s_j(\mathbf{p}, \mathbf{v})$ for a single ellipsoid in (11), (8) and (9), respectively. If $\mathbf{p} \in \mathcal{E}_j$, then $s_j(\mathbf{p}, \mathbf{v}) \leq 0$. Hence, to determine whether \mathbf{p} is contained in any ellipsoid, we can find the minimum $s_j(\mathbf{p}, \mathbf{v})$. When a ray (\mathbf{p}, \mathbf{v}) intersects an ellipsoid, we have $i_j(\mathbf{p}, \mathbf{v}) \geq 0$. Hence, to determine whether any ellipsoid is intersected, we can find the maximum $i_j(\mathbf{p}, \mathbf{v})$. Finally, the SDDF of a union of ellipsoids is equal to the minimum of the individual ellipsoid SDDFs but with the intersected ellipsoids prioritized. In summary, the intersection indicator, the sign indicator, and the SDDF value of a union of M ellipsoids are:

$$i(\mathbf{p}, \mathbf{v}; \cup_j \mathcal{E}_j) = \max_j i_j(\mathbf{p}, \mathbf{v}), \quad (13)$$

$$s(\mathbf{p}, \mathbf{v}; \cup_j \mathcal{E}_j) = \min_j s_j(\mathbf{p}, \mathbf{v}), \quad (14)$$

$$f(\mathbf{p}, \mathbf{v}; \cup_j \mathcal{E}_j) = \begin{cases} \min_{j: i_j(\mathbf{p}, \mathbf{v}) \geq 0} f_j(\mathbf{p}, \mathbf{v}), & \exists i_j(\mathbf{p}, \mathbf{v}) \geq 0, \\ \min_j f_j(\mathbf{p}, \mathbf{v}), & \text{otherwise.} \end{cases} \quad (15)$$

Thus, given M ellipsoids with pose and radii $\mathbf{T}_j, \mathbf{r}_j$ for $1 \leq j \leq M$, we define our ellipsoid-based prior network as:

$$(i, s, f, j_f) = P(\mathbf{p}, \mathbf{v} \mid \{\mathbf{T}_j, \mathbf{r}_j\}_{j=1}^M), \quad (16)$$

where j_f is the index of the ellipsoid selected by (15). This ellipsoid index is used to condition the latent feature computation, which will be described in Sec. V. We refer to P in (16) as a network because its outputs are differentiable with respect to $\mathbf{p}, \mathbf{v}, \mathbf{T}_j$, and \mathbf{r}_j . We provide the analytical gradients in Appendix A-B.

Because our prior network uses ellipsoids to approximate SDDF, it satisfies the Eikonal equation in (4) by construction.

Proposition 3. *The SDDF $f(\mathbf{p}, \mathbf{v}; \cup_j \mathcal{E}_j)$ in (15) computed by the ellipsoid-based prior network satisfies the SDDF directional Eikonal equation in (4).*

Proof: Please refer to Appendix A-C. ■

The network P provides a coarse geometric prior but does not yield accurate predictions. We address this next.

V. RESIDUAL NETWORK

In this section, we design a residual network to predict a correction term $\delta_f(\mathbf{p}, \mathbf{v})$ so that the SDDF prediction of our combined prior and residual model, $\hat{f}(\mathbf{p}, \mathbf{v}) = f(\mathbf{p}, \mathbf{v}) + \delta_f(\mathbf{p}, \mathbf{v})$, is accurate even for sets with complicated shapes. Intuitively, we expect the prior network P to learn the rough shape of the environment, encoded in $f(\mathbf{p}, \mathbf{v})$, while the residual network R captures the details, encoded in $\delta_f(\mathbf{p}, \mathbf{v})$.

A. Latent Feature Network

The residual network needs to estimate the SDDF correction term $\delta_f(\mathbf{p}, \mathbf{v})$ based on the local shape of the surface that the ray (\mathbf{p}, \mathbf{v}) interacts with. We convert \mathbf{p} and \mathbf{v} to the local coordinate frame of the first intersected ellipsoid and train a latent feature network whose output \mathbf{z} is decoded into a SDDF correction by a residual decoder network $\delta_f = R(\mathbf{z})$.

Given a ray (\mathbf{p}, \mathbf{v}) , the prior network in (16) provides (i, s, f) and the index j_f of the selected ellipsoid. Using the pose of the j_f -th ellipsoid $\mathbf{R}_{j_f} \in SO(3)$, $\mathbf{c}_{j_f} \in \mathbb{R}^3$, we obtain the intersection point \mathbf{q} in the ellipsoid frame:

$$\mathbf{q} = \mathbf{R}_{j_f}^\top (\mathbf{p}_{j_f} + f\mathbf{v} - \mathbf{c}_{j_f}) = \mathbf{p}' + f\mathbf{v}'. \quad (17)$$

We train a latent feature network $\mathbf{z} = L(\mathbf{q}, \mathbf{v}', j_f)$ with the intersection point \mathbf{q} , local viewing direction \mathbf{v}' , and ellipsoid index j_f as input and a latent feature \mathbf{z} as output.

We observe that the ellipsoid SDDF in (7) can be expanded as a multivariate polynomial, where each variable's maximum degree is 2. Inspired by this observation, we design the network L to transform a polynomial embedding vector into a latent feature vector:

$$\mathbf{z} = L(\mathbf{q}, \mathbf{v}', j_f \mid \{\mathbf{W}_i\}_{i=1}^M) = \mathbf{W}_{j_f} \mathbf{m} \in \mathbb{R}^m, \quad (18)$$

$$\mathbf{m} = \text{vec}(E(\mathbf{q})E(\mathbf{v}')^\top) \in \mathbb{R}^{100}, \quad (19)$$

$$E(\mathbf{p}) = [p_x^2, p_x p_y, p_x p_z, p_y^2, p_y p_z, p_z^2, p_x, p_y, p_z, 1]^\top, \quad (20)$$

where $E: \mathbb{R}^3 \rightarrow \mathbb{R}^{10}$ is a degree-2 monomial embedding, $\text{vec}(\cdot)$ concatenates the columns of the input matrix, \mathbf{m} is a vector of degree-2 monomials, and $\mathbf{W}_i \in \mathbb{R}^{m \times 100}$.

B. Residual Decoder

The residual decoder is a multi-layer perceptron $R: \mathbb{R}^m \rightarrow \mathbb{R}^3$ that decodes the latent feature vector $\mathbf{z} \in \mathbb{R}^m$ into three residual predictions $(\delta_i, \delta_s, \delta_f)$. Then, the final predictions of the intersection indicator, sign indicator, and SDDF value are

$$\hat{i}(\mathbf{p}, \mathbf{v}) = \tanh(\alpha i(\mathbf{p}, \mathbf{v})) + \delta_i(\mathbf{p}, \mathbf{v}), \quad (21)$$

$$\hat{s}(\mathbf{p}, \mathbf{v}) = \tanh(\alpha s(\mathbf{p}, \mathbf{v})) + \delta_s(\mathbf{p}, \mathbf{v}), \quad (22)$$

$$\hat{f}(\mathbf{p}, \mathbf{v}) = f(\mathbf{p}, \mathbf{v}) + \delta_f(\mathbf{p}, \mathbf{v}), \quad (23)$$

where $\alpha > 0$ is a hyperparameter. Since the prior network produces $i(\mathbf{p}, \mathbf{v}) \in \mathbb{R}$ and $s(\mathbf{p}, \mathbf{v}) \in \mathbb{R}$ but, as described later in Sec. VI-A, we provide supervision $i^*(\mathbf{p}, \mathbf{v}) \in \{-1, 1\}$ and $s^*(\mathbf{p}, \mathbf{v}) \in \{-1, 1\}$ for (21) and (22), we use \tanh to squash the output of the prior intersection indicator and sign indicator. The residuals δ_i and δ_s are applied after the squashing to prevent clipping their gradients during training.

Complementing Proposition 3, we show that the joint prior-residual SDDF prediction \hat{f} in (23) still satisfies the SDDF directional Eikonal equation by construction.

Proposition 4. *The SDDF $\hat{f}(\mathbf{p}, \mathbf{v})$ in (23) computed by the combination of the prior and the residual networks satisfies the SDDF directional Eikonal equation in (4).*

Proof: Please refer to Appendix B-A. ■

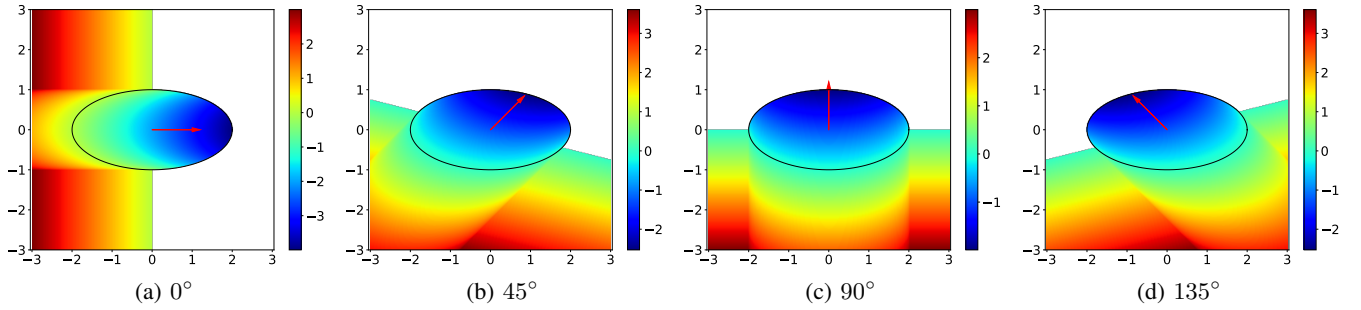


Fig. 4: 2D visualization of the single ellipsoid SDDF $f(\mathbf{p}, \mathbf{v}; \mathcal{E})$ in (11) for fixed \mathbf{v} and varying \mathbf{p} .

Because our SDDF model satisfies the Eikonal equation by construction, we do not need an extra loss term to regularize the network and can use fewer parameters in the model, making it more efficient to train.

VI. TRAINING

A. Dataset Generation and Augmentation

We convert the sensor poses and range measurements $\{\mathbf{T}_t, \mathcal{Z}_t\}_{t=1}^T$, $\mathcal{Z}_t = \{\mathbf{v}_i, r_{t,i}\}_{i=1}^N$, described in Sec. III, into a dataset $\mathcal{D} = \{\mathbf{p}_j, \mathbf{v}_j, f_j^*, i_j^*, s_j^*\}_j$ suitable for training our SDDF model. Here, $\mathbf{p}_j \in \mathbb{R}^3$ is the origin of the ray, $\mathbf{v}_j \in \mathbb{S}^2$ is the direction of the ray provided in \mathcal{Z}_t , f_j^* is an SDDF measurement, $i_j^* \in \{-1, 1\}$ is an intersection indicator measurement, and $s_j^* \in \{-1, 1\}$ is a sign indicator measurement. From each ray measurement $\mathbf{v}_i, r_{t,i}$, obtained from sensor position \mathbf{p}_t and orientation \mathbf{R}_t , we generate a corresponding data sample as $\mathbf{p}_j = \mathbf{p}_t$, $\mathbf{v}_j = \mathbf{R}_t \mathbf{v}_i$, $f_j^* = r_{t,i}$, $i_j^* = 1$, $s_j^* = 1$. These data are unbalanced in the sign indicator and the SDDF sign because all the samples have $s_j^* = 1$ and $f_j^* \geq 0$. Therefore, we need to augment the data with negative samples. For each sample $(\mathbf{p}_j, \mathbf{v}_j, f_j^*, i_j^*, s_j^*)$, we generate a corresponding negative sample $(\mathbf{p}', \mathbf{v}_j, -\epsilon, 1, -1)$, where we extend the ray to a point $\mathbf{p}' = \mathbf{p}_j + (f_j^* + \epsilon)\mathbf{v}_j$ slightly behind the observed surface with a small offset $\epsilon > 0$. Although the intersection indicator i_j^* is also unbalanced, it is inefficient to generate non-intersecting rays, and our experiments show that augmenting the intersection indicator does not improve our reconstruction results.

B. Ellipsoid Initialization

We present an initialization strategy for the M ellipsoids, needed by the ellipsoid-based prior network P in Sec. IV. Using the augmented dataset \mathcal{D} constructed above, we obtain a point cloud:

$$\mathcal{X} = \{\mathbf{x}_k\}_{k=1}^K = \{\mathbf{p}_j + f_j^* \mathbf{v}_j \mid f_j^* \geq 0\}_j \cup \{\mathbf{p}_j \mid f_j^* < 0\}_j,$$

which is the collection of surface points and points inside obstacles. Leaving the number of ellipsoids M as a hyperparameter, we use K-means++ [2] to divide \mathcal{X} into M clusters $\{\mathcal{X}_m\}_{m=1}^M$. For each cluster, we initialize an ellipsoid using principal component analysis of the points in the cluster as shown in Alg. 1. In practice, we set a minimum allowed radius $r_{\min} = 0.005$ to avoid numerical problems and scale the

Algorithm 1 Single Ellipsoid Initialization

- 1: **procedure** SINGLEELLIPSOIDINIT($\mathcal{X} = \{\mathbf{x}_k\}_{k=1}^K$)
- 2: $\mathbf{c} \leftarrow \frac{1}{K} \sum_{k=1}^K \mathbf{x}_k$ ▷ center
- 3: $\mathbf{X} \leftarrow [\mathbf{x}_1 \cdots \mathbf{x}_K]^\top - \mathbf{1}\mathbf{c}^\top$
- 4: Eigen decomposition on $\frac{1}{K} \mathbf{X}^\top \mathbf{X} = \mathbf{Q}\mathbf{\Lambda}\mathbf{Q}$
- 5: $\mathbf{R} \leftarrow \mathbf{Q} \text{diag}([1 \cdots \det \mathbf{Q}])$ ▷ rotation
- 6: $[\lambda_1 \cdots \lambda_n] \leftarrow \text{diag}(\mathbf{\Lambda})$ ▷ n is the space dimension
- 7: $r_i \leftarrow \max(r_{\min}, \alpha \sqrt{|\lambda_i|})$ ▷ radii
- 8: **return** $\mathbf{R}, \mathbf{c}, \mathbf{r}$

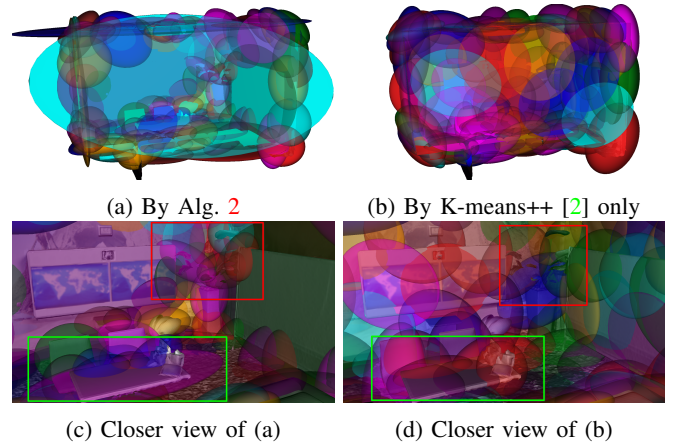


Fig. 5: Comparison of ellipsoid initialization algorithms. The left column is generated by Alg. 2 and the right column is by the K-means++ [2] algorithm only (i.e. L3 to L5 of Alg. 2). (a) Using Alg. 2, a few ellipsoids are used to approximate planar surfaces like ceiling, wall, and ground. (b) Using K-means++ [2] only, too many ellipsoids are used to approximate planar surfaces. (c) and (d) show close-ups of the indoor objects. The table (in the green box) and the plant (in the red box) are better approximated by ellipsoids from Alg. 2.

ellipsoids by $\alpha = 3$ to ensure that the points \mathcal{X}_m are mostly covered by the m -th ellipsoid.

However, in typical indoor environments, as shown in Fig. 5, this approach allocates too many ellipsoids to planar surfaces, which could be fit by a single flat ellipsoid. Hence, we propose Alg. 2 to create a better multi-ellipsoid initialization. After using K-means++ [2] to divide \mathcal{X} into M clusters and create an ellipsoid $(\mathbf{R}_m, \mathbf{c}_m, \mathbf{r}_m)$ for each cluster m by Alg. 1, we build an undirected graph $\mathcal{G} = (\mathcal{V}, \mathcal{E})$ where each node is a

Algorithm 2 Multi-Ellipsoid Initialization

```

1: procedure MULTIELLIPSOIDINIT( $\mathcal{X} = \{\mathbf{x}_k\}_{k=1}^K, M, S$ )
2:    $\triangleright S$  is the number of ellipsoid neighbors
3:    $\{\mathcal{X}_m\}_{m=1}^M \leftarrow \text{K-MEANS++}(\mathcal{X}, M)$ 
4:   for  $m = 1 \dots M$  do
5:      $\mathbf{R}_m, \mathbf{c}_m, \mathbf{r}_m \leftarrow \text{SINGLEELLIPSOIDINIT}(\mathcal{X}_m)$ 
6:      $j \leftarrow \arg \min_{1 \leq j \leq n} r_{m,j}$ 
7:      $\mathbf{n}_m \leftarrow \mathbf{R}_m \mathbf{e}_j$ 
8:      $\beta_m \leftarrow \frac{1}{|\mathcal{X}_m|} \sum_{\mathbf{p} \in \mathcal{X}_m} \mathbf{n}_m^\top (\mathbf{p} - \mathbf{c}_m)$ 
9:    $\mathcal{V} \leftarrow \emptyset, \mathcal{E} \leftarrow \emptyset$   $\triangleright$  undirected graph
10:  for  $i = 1 \dots M, \beta_i < \beta_{\max}$  do  $\triangleright$  flat ellipsoid
11:     $\mathcal{K}_i \leftarrow \text{K-NEARESTNEIGHBOR}(\{\mathbf{c}_m\}_{m=1}^M, i, S)$ 
12:    for  $j \in \mathcal{K}_i, \beta_j < \beta_{\max}$  do
13:       $\eta \leftarrow \frac{1}{2} (|(\mathbf{c}_i - \mathbf{c}_j)^\top \mathbf{n}_i| + |(\mathbf{c}_i - \mathbf{c}_j)^\top \mathbf{n}_j|)$ 
14:      if  $\eta < \eta_{\max}$  then  $\triangleright i$  and  $j$  are coplanar
15:         $\mathcal{V} \leftarrow \mathcal{V} \cup \{i, j\}$  and  $\mathcal{E} \leftarrow \mathcal{E} \cup \{(i, j)\}$ 
16:     $\{\mathcal{V}_i\}_{i=1}^C \leftarrow \text{FINDCONNECTEDCOMPONENTS}(\mathcal{V}, \mathcal{E})$ 
17:     $\mathcal{R} \leftarrow \emptyset, \mathcal{X}' \leftarrow \emptyset$ 
18:    for  $i = 1 \dots C$  do  $\triangleright$  merge ellipsoids
19:       $\mathbf{R}, \mathbf{c}, \mathbf{r} \leftarrow \text{SINGLEELLIPSOIDINIT}(\bigcup_{m \in \mathcal{V}_i} \mathcal{X}_m)$ 
20:       $\mathcal{R} \leftarrow \mathcal{R} \cup \{(\mathbf{R}, \mathbf{c}, \mathbf{r})\}$ 
21:       $\mathcal{X}' \leftarrow \mathcal{X}' \cup \bigcup_{m \in \mathcal{V}_i} \mathcal{X}_m$ 
22:     $\{\mathcal{X}'_m\}_{m=1}^{M-C} \leftarrow \text{K-MEANS++}(\mathcal{X} - \mathcal{X}', M - C)$ 
23:    for  $m = 1 \dots M - C$  do  $\triangleright$  initialize other ellipsoids
24:       $\mathbf{R}, \mathbf{c}, \mathbf{r} \leftarrow \text{SINGLEELLIPSOIDINIT}(\mathcal{X}'_m)$ 
25:       $\mathcal{R} \leftarrow \mathcal{R} \cup \{(\mathbf{R}, \mathbf{c}, \mathbf{r})\}$ 
26:  return  $\mathcal{R}$   $\triangleright M$  ellipsoid poses and radii

```

flat ellipsoid $i \in \mathcal{V}$ (i.e. the mean projection β of $\mathbf{x}_k \in \mathcal{X}_m$ to the shortest axis is smaller than threshold β_{\max}), and two nodes (i, j) are connected only when they are coplanar neighbors. Then, we find the number of ellipsoids, C , for these planar surfaces by finding the connected components $\{\mathcal{V}_i\}_{i=1}^C$ of \mathcal{G} . We merge the ellipsoids in each component \mathcal{V}_i running Alg. 1 on $\bigcup_{m \in \mathcal{V}_i} \mathcal{X}_m$. Finally, the remaining points $\bigcup_{m \notin \mathcal{V}} \mathcal{X}_m$ are divided into $M - C$ clusters by K-means++ [2] and the ellipsoid of each cluster is initialized by Alg. 1. As shown in Fig. 5, the planar surfaces are correctly detected and approximated by only a few ellipsoids, leaving more ellipsoids for other more complex shapes.

C. Loss Function for Ellipsoid-based Prior Network

Given a prediction $\mathbf{x} = (i, s, f)$ from the ellipsoid-based prior network P and the corresponding label $\mathbf{x}^* = (i^*, s^*, f^*)$ from the measurement data \mathcal{D} , we compute a weighted sum of Huber losses:

$$\begin{aligned}
l_0(x, y) &= \begin{cases} 0.5(x - y)^2, & \text{if } |x - y| < 1, \\ |x - y| - 0.5, & \text{otherwise,} \end{cases} \\
l(x, y) &= (w^+ \mathbb{1}(y \geq 0) + w^- \mathbb{1}(y < 0)) l_0(x, y), \\
\mathcal{L}_P(\mathbf{x}, \mathbf{x}^*) &= l(i, i^*) + l(s, s^*) + l(f, f^*).
\end{aligned} \tag{24}$$

The role of P is to make the ellipsoids cover the objects in the scene so that the occlusions between objects are captured. Thus, larger weights are used for negative f^* and negative s^* : $w_f^- = 1.65$ and $w_s^- = 10$. The other weights are set to 1.

D. Loss Function for Residual Network

The residual network is trained using the same loss function as the prior network in (24) but with different weights. Unlike the prior network, the residual network focuses on learning the geometric details. Thus, higher weights are used for the SDDF prediction \hat{f} . Given the prediction $\hat{\mathbf{x}} = (\hat{i}, \hat{s}, \hat{f})$ and the corresponding label $\mathbf{x}^* = (i^*, s^*, f^*)$ from the measurement data \mathcal{D} , we have

$$\begin{aligned}
\mathcal{L}_R(\hat{\mathbf{x}}, \mathbf{x}^*) &= l(\hat{i}, i^*) + l(\hat{s}, s^*) + l(\hat{f}, f^*), \\
\mathcal{L}(\hat{\mathbf{x}}, \mathbf{x}, \mathbf{x}^*) &= \mathcal{L}_P(\mathbf{x}, \mathbf{x}^*) + \mathcal{L}_R(\hat{\mathbf{x}}, \mathbf{x}^*),
\end{aligned} \tag{25}$$

where for \mathcal{L}_R , $w_{\hat{f}}^+ = 1.0$, $w_{\hat{f}}^- = 1.1$, and other weights 0.1.

VII. APPLICATION TO VIEWPOINT OPTIMIZATION

Our SDDF model is differentiable and, hence, enables continuous viewpoint optimization, which can be used, for example, to explore an unknown environment. For simplicity, we first consider determining the next-best view and then scale up to optimization of a trajectory of several views.

Our SDDF model can predict a point cloud measurement from any desired sensor pose $(\mathbf{p}_t, \mathbf{R}_t)$ as:

$$\mathcal{P}_t = \{\mathbf{p}_t + \hat{f}_i \mathbf{R}_t \mathbf{v}_i\}_{i=1}^N, \tag{26}$$

where $\{\mathbf{v}_i\}_{i=1}^N$ are the ray directions in the sensor frame and \hat{f}_i are the SDDF predictions for each ray. The utility of a point-cloud measurement for the purpose of exploration or environment coverage can be evaluated in terms of the visible region volume. We use the following loss to measure the (negative) size of the visible volume:

$$\mathcal{L}_v(\{\hat{f}_i\}_{i=1}^N) = -\frac{1}{2N} \sum_{i=1}^N (\max\{\hat{f}_i, 0\})^2. \tag{27}$$

Moreover, consecutive measurements \mathcal{P}_t and \mathcal{P}_{t+1} should have a small overlap in order to observe a large area. Therefore, we design the following overlap loss:

$$\mathcal{L}_o(\mathcal{P}_t, \mathcal{P}_{t+1}) = -\frac{\sum_{\mathbf{p} \in \mathcal{P}_t, \mathbf{q} \in \mathcal{P}_{t+1}} \min\{\|\mathbf{p} - \mathbf{q}\|_2, d_{\max}\}}{|\mathcal{P}_t| |\mathcal{P}_{t+1}|}, \tag{28}$$

where $d_{\max} > 0$ is a distance threshold of no overlap.

Additionally, we must also ensure that the sensor is not in collision with any obstacles. To do so, we introduce a set of risk detection rays, which are uniformly sampled from the sphere that contains the robot, and obtain their SDDF predictions $\{\hat{f}_i^r\}_{i=1}^M$. The risk loss is defined as:

$$\mathcal{L}_r(\{\hat{f}_i^r\}_{i=1}^M) = \frac{1}{M} \sum_{i=1}^M \max\{d_{\text{safe}} - \hat{f}_i^r, 0\}, \tag{29}$$

where $d_{\text{safe}} > 0$ is a safe distance threshold, chosen such that $\hat{f}_i^r < d_{\text{safe}}$ implies a potential collision.

We optimize the camera pose $(\mathbf{p}_{t+1}, \mathbf{R}_{t+1})$ at time $t + 1$ by minimizing the weighted sum $\mathcal{L} = w_o \mathcal{L}_o + w_v \mathcal{L}_v + w_r \mathcal{L}_r$, where w_o , w_v , and w_r are weights.

There are many ways to scale this method up to viewpoint trajectory optimization. It is inefficient to optimize every pose

on the trajectory because two views that are close to each other are very likely to overlap significantly, and the robot kinematic constraints may not allow much adjustment for the viewpoint. Therefore, we suggest optimizing certain waypoints on the trajectory. We incrementally optimize n poses $\{\mathbf{p}_i, \mathbf{R}_i\}_{i=0}^n$ generated by an off-the-shelf planning algorithm, such as RRT* [17], such that for each pose $\{\mathbf{p}_i, \mathbf{R}_i\}_{i>0}$, we optimize the loss:

$$\mathcal{L}' = w_o \mathcal{L}_o \left(\mathcal{P}_0 \bigcup_{j=1}^{j<i} \mathcal{P}'_j, \mathcal{P}_i \right) + w_v \mathcal{L}_v + w_r \mathcal{L}_r, \quad (30)$$

where \mathcal{P}'_j is the predicted point cloud at optimized waypoint $(\mathbf{p}'_j, \mathbf{R}'_j)$.

During the optimization, we downsample $\mathcal{P}_0 \bigcup_{j=1}^{j<i} \mathcal{P}'_j$ with a stride of $i-j$, labeled as $\tilde{\mathcal{P}}_j$, such that $\tilde{\mathcal{P}}_j$ has a constant size. This incremental optimization strategy provides two benefits. First, it reduces the use of GPU memory and makes the along-trajectory multi-view optimization problem solvable. Second, it allows the robot to parallelize the trajectory optimization and execution.

VIII. EVALUATION

We evaluate our SDDF model in terms of accuracy, computational efficiency, and usefulness for viewpoint optimization. First, we compare against three state-of-the-art baselines on synthetic and real datasets. Then, an ablation study examines the effectiveness of each module in our model by varying the number of ellipsoids, data augmentation and initialization strategies, and the use of polynomial embedding. Finally, we demonstrate the utility of SDDF in viewpoint optimization.

A. Comparison with Baselines

Baselines: We compare our method against three baselines: Nerfacto [38], RaDe-GS [46], and SDF-Instant-NGP [26]. These methods were not initially designed for SDDF prediction but can be used to predict SDDF as follows. For SDF, we implement sphere tracing [11] to find the closest point on the surface along the query direction. For Nerfacto and RaDe-GS, we render a depth image at the query viewpoint, project the depth image to a point cloud, and compute the distance. We compare the mean absolute error (MAE) in SDDF prediction and the computational cost in terms of GPU memory, model size, and inference time.

Datasets: A total of 14 synthesized and one real datasets are used for comparison. We obtained data from six scenes from Replica (“Hotel” and “Office 0-5”) [36], the Allensville scene from Gibson [42], and scene 0000-00 from ScanNet [7].

From the seven synthetic scenes, we synthesize two sensor types, LiDAR and RGB-D, for a total of 14 datasets. For both sensor types, measurements are synthesized from a grid of free space positions in the scene. LiDAR data is synthesized with 360 horizontal and 180 vertical angular increments, ranging between $[-\pi, \pi] \times [-\pi/2, \pi/2]$. RGB-D data is synthesized from six uniform camera orientations, with an image resolution of 640×480 , and horizontal and vertical fields of view of

$94^\circ \times 77^\circ$. For each scene, we sample 20 random test viewpoints (40 for Allensville), which were visually confirmed to be representative of possible camera poses in real applications.

ScanNet [7] provides real RGB-D images captured along a trajectory. During training, the RGB images are linearly interpolated to align with the depth images of resolution 640×480 . We found the quality of the reference mesh from ScanNet is insufficient for generating SDDF ground truths, and used this dataset for qualitative comparison only. The views for comparison are generated by randomly selecting and perturbing waypoints of the trajectory ($\mathcal{U}_{[-0.2, 0.2]}$ for each dimension of the translation, and $\mathcal{U}_{[-\pi, \pi]}$ for the yaw angle) so that the rendered views are representative.

Experiment Setup: The LiDAR and RGB-D datasets are used as follows. For our method, we consider both the LiDAR and RGB-D cases. When using the RGB-D datasets with our method, we only use the depth images, and apply $20 \times$ downsampling ($5 \times$ for Replica Hotel), to achieve similar ray density as the LiDAR dataset. Similarly, for SDF-Instant-NGP, we consider both LiDAR and RGB-D datasets, and use all range measurements in either the LiDAR or depth images, along with additional data augmentations of near-surface samples and free-space samples necessary for stable training [26]. For Nerfacto and RaDe-GS, we only consider the RGB-D case, as they do not support rendering LiDAR data. RaDe-GS is trained with and without RGB (i.e., either depth-only or RGB-D), whereas Nerfacto is only trained with RGB-D, as RGB is necessary for training Nerfacto. RaDe-GS is trained with $2 \times$ downsampling due to GPU memory limitation, and Nerfacto is trained using the full dataset.

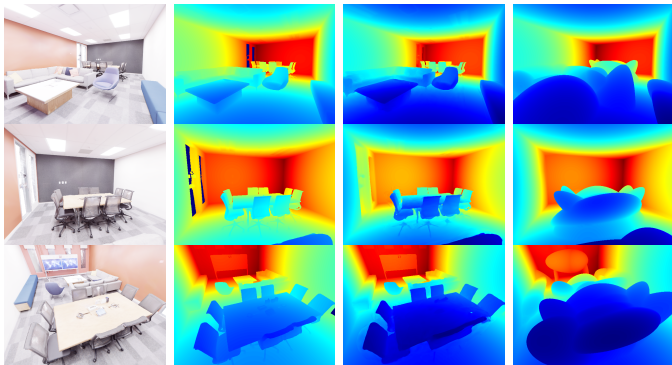
Our method uses 128 ellipsoids (256 for Gibson Allensville) to fit an SDDF prior of the scene. In contrast, RaDe-GS uses 5% of the range measurements (3% for Allensville due to GPU memory limit) to initialize one Gaussian per each measurement, which yields many more Gaussians than our ellipsoids. Further training details are provided in Appendix C.

Accuracy of SDDF Predictions: We first compare the SDDF predictions made using different methods. Qualitative results are shown in Figs. 6c and 7 (more results in Figs. 10-12 in Appendix D). Our SDDF model accurately learns the geometry of the scene, as shown in the three qualitative examples in Fig. 6. The overall model remains robust to varying viewing distances because the latent feature for the residual network is constructed from the intersection point and the viewing direction in a way that satisfies the Eikonal constraint (Proposition 4). The ellipsoidal prior (Fig. 6d) is optimized to approximate the shapes of objects in the scene, based on which the residual network recovers fine details with high fidelity, as seen in Fig. 6c. This ellipsoid-based network design allows readily combining different sensor measurements of the same surface into a neural representation.

Fig. 7 shows qualitative comparisons against RaDe-GS [46] (RGB-D and depth-only), Nerfacto [38], and SDF-Instant-NGP [26] with sphere tracing. In Fig. 7c, RaDe-GS exhibits erroneous artifacts around the toilet, at the corner, or near the fridge, where there are limited RGB-D observations.

TABLE I: Mean absolute error (cm) of SDDF prediction

		Allensville	Hotel	Office 0	Office 1	Office 2	Office 3	Office 4
LiDAR	SDF-Instant-NGP [26]	1.137	1.224	0.825	0.724	1.342	1.608	1.037
	SDDF (ours)	1.350	0.997	1.092	0.694	1.236	1.588	1.132
RGB-D	RaDe-GS [46]	1.737	0.857	0.438	0.348	1.258	0.827	0.498
	Nerfacto [38]	83.433	58.272	63.011	68.382	69.144	74.168	88.479
Depth Only	RaDe-GS (w/o RGB) [46]	25.002	45.948	1.208	6.654	3.582	0.955	0.500
	SDF-Instant-NGP [26]	1.106	1.297	0.737	0.711	1.120	1.395	0.953
	SDDF (ours)	1.490	1.247	1.120	0.696	1.081	1.568	1.206



(a) Scene (b) SDDF G.T. (c) Prediction (d) SDDF Prior

Fig. 6: SDDF prediction by our method. Columns a) and b) show RGB images and ground-truth SDDF. As shown in c), our model remains accurate with varying view distance due to satisfying the directional Eikonal constraint. As shown in d), the ellipsoidal prior provides a coarse approximation of the shape of objects in the scene, such as walls, chairs, and tables to be used by the residual network.

Meanwhile, our method accurately reconstructs these areas. Nerfacto also exhibits artifacts due to insufficient data as shown in Fig. 7e. Since no explicit representations like our ellipsoids or the Gaussians in RaDe-GS are used, Nerfacto predicts SDDF based on the learned volume density, which is optimized for photometric rendering rather than scene geometry, leading to large distance prediction errors.

Meanwhile, sphere tracing on SDF-Instant-NGP [26] does not exhibit significant artifacts. However, this baseline tends to learn smoother shapes that lack sharper details, such as the plant shown in the second row or the chairs in the third row of Fig. 7f. Moreover, the first row of Fig. 7f shows that the errors accumulated during sphere tracing become significant at boundaries when the SDF model does not predict accurate SDF consistently. These qualitative observations are consistent in *real* ScanNet data [7], as shown in Figs. 7 and 12.

The quantitative results in Table I show that our method reaches the state of the art for both LiDAR and RGB-D datasets. Our method has slightly higher errors on RGB-D datasets because our method only uses depth information from the RGB-D datasets, whereas RaDe-GS uses both RGB and depth data. Moreover, our method is trained with $20\times$ downsampling, whereas RaDe-GS uses $2\times$ downsampling and hence approximately $10\times$ more depth data. Consequently, RaDe-GS uses a significantly higher number of parameters

TABLE II: Max. GPU memory usage, model size, and inference time on Replica-Hotel dataset [36] (Intel 14900K CPU and NVIDIA RTX-3090 GPU).

	SDDF	RaDe-GS	Nerfacto	SDF
Training GRAM (G)	3.3	18.7	4.7	6.2
Testing GRAM (G)	1.7	6.7	3.6	1.8
No. Parameters (M)	2.7	113.7	16.4	1.7
Inference Time (ms/per frame)	69	7	254	103

as seen in Table II. Nerfacto and SDF-Instant-NGP do not downsample the data, but generally perform worse than ours. With RGB-D datasets, RaDe-GS [46] has the lowest MAE among models that use both RGB and depth. However, as shown in Table I and in Fig. 7d, when RaDe-GS is trained using depth data only, it shows significantly larger errors in larger and more complicated scenes. We omit quantitative evaluation on ScanNet data (Fig. 12), due to the unavailability of a reliable ground-truth mesh.

Computational Efficiency: Table II shows the computational cost of all methods, in terms of inference time, number of parameters, and maximum GPU memory usage during training and testing. Our method exhibits the lowest memory usage for training and testing, and the second lowest number of parameters after SDF-Instant-NGP [26]. This is because we use much fewer ellipsoids than Gaussians in RaDe-GS [46], which has the highest GPU memory usage. The lower GPU memory usage of our method is beneficial for scaling up to larger scenes, or deployment on mobile robots with limited hardware resources. Although Nerfacto has relatively low GPU memory usage, it has the longest inference time, and its prediction error is much higher than other methods.

In terms of computation time, our method is the second best, with RaDe-GS significantly outperforming our method. We attribute this to the highly optimized, full-CUDA implementation of RaDe-GS, and expect to achieve similar performance with improvements in the implementation. Our method is $1.5\times$ faster than the SDF-Instant-NGP-based sphere-tracing method, and $4\times$ faster than Nerfacto. This is because our method only requires a single forward pass, whereas the other methods require multiple passes. It is also worth noting that our method is faster than the SDF-Instant-NGP despite their CUDA optimized implementation. This shows that our method has good potential in terms of computation speed.

B. Ablation Study

We examine the performance of our model in four variations. We first consider using twice or half the number of

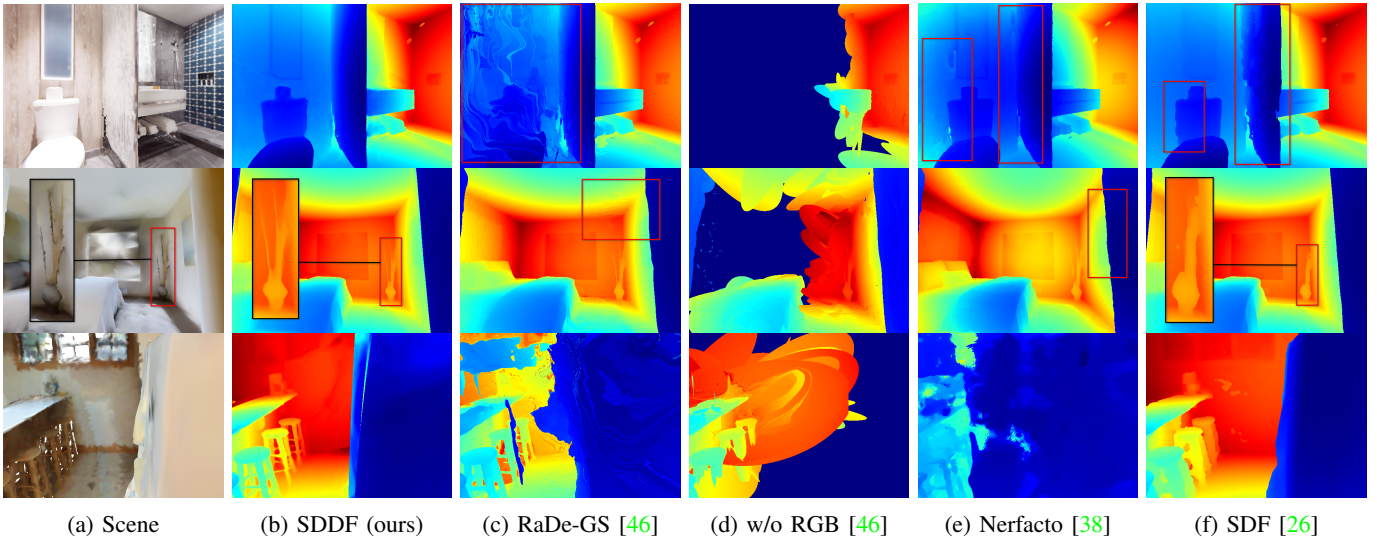


Fig. 7: Qualitative comparison of SDDF predictions. Row 1: Replica Hotel (synthesized). Row 2: Gibson Allensville (synthesized). Row 3: ScanNet scene 0000-00 (real). In areas with limited sensor measurements, RaDe-GS [46] fails to learn the geometry, with RGB (c) or without RGB (d), yielding artifacts. Nerfacto [38] in e) shows significant artifacts and large distance prediction error. SDF-Instant-NGP [26] in f) tends to learn a smoother approximation, missing sharp boundaries.

TABLE III: Ablation experiments on LiDAR datasets. Mean absolute error (cm) of SDDF prediction is reported.

	Allensville	Hotel	Office 0	Office 1	Office 2	Office 3	Office 4
twice number of ellipsoids	1.414	1.013	1.034	0.716	1.291	1.649	1.250
half number of ellipsoids	1.477	1.013	1.072	0.706	1.218	1.727	1.192
without negative samples	5.379	2.639	1.954	0.867	2.734	8.598	2.406
K-means++ [2] only ellipsoid initialization	1.405	1.033	1.060	0.703	1.279	1.636	1.248
Fourier embedding	1.842	1.303	1.544	0.930	1.771	2.513	1.631
default	1.350	0.997	1.092	0.694	1.236	1.588	1.132

ellipsoids for each scene. To investigate the contribution of negative samples augmentation, we compare against a SDDF model trained without negative samples. In addition, we train SDDF models with ellipsoids initialized by K-means++ [2] only. To demonstrate the benefit of the polynomial embedding, we compare against using the Fourier embedding [37]. The results are summarized in Table III.

Table III shows that although our method is robust to the number of ellipsoids, using too few or too many ellipsoids causes problems. With too few ellipsoids, the model cannot approximate the shape of objects in the scene well, whereas with too many ellipsoids, the model learns spurious occlusions between the ellipsoids. During testing, we also found that too many ellipsoids cause the optimizer to move some redundant ellipsoids out of the scene.

Negative SDDF sample augmentation plays a key role in optimizing ellipsoids. Fig. 8 shows that with negative SDDF samples, the ellipsoid priors are optimized to cover the scene well. In contrast, without negative samples, the resulting ellipsoids are generally smaller and regress into the interior of objects, which leads to missing ray intersections. Missing ray intersections cause a wrong ellipsoid to be selected at a further location, leaving the burden to the residual decoder R to learn larger residuals.

Appropriate ellipsoid initialization is also important. As

shown in Table III, initializing the ellipsoids solely with K-means++ [2] causes larger errors, as K-means++ generally uses an excessive number of ellipsoids for planar surfaces.

We also consider using the Fourier embedding [37] in place of the polynomial embedding introduced in this work. The Fourier embedding may seem useful because it can learn high-frequency features. However, the results in Table III show that polynomial embedding provides better generalization for different scenes with smaller errors. Our investigation indicates that this is because the Fourier embedding requires different spatial frequency hyperparameters for each scene to achieve comparable performance, whereas the polynomial embedding does not require such hyperparameter tuning.

C. Application to Viewpoint Optimization

The first row of Fig. 9 demonstrates gradient-based next-best view optimization using our SDDF model. The visualization shows that our method can reduce the overlap between the two camera views and increase the observed area. In this example, the area observed by the two camera views increases to $36.15m^2$ (+90.3%) from $19.00m^2$ with the initial viewpoints. In the second row of Fig. 9, we show an example of scaling up to a trajectory. By optimizing the waypoints, the observed area increases from $124.55m^2$ to $177.50m^2$ (+37.7%).

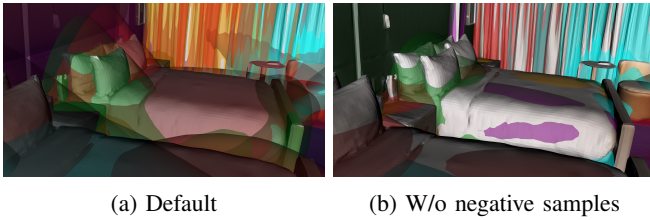


Fig. 8: Ablation study of negative samples augmentation. With negative sample augmentation in (a), the ellipsoids cover the objects in the scene. Without negative sample augmentation (b), the objects are not covered by ellipsoids in many places.

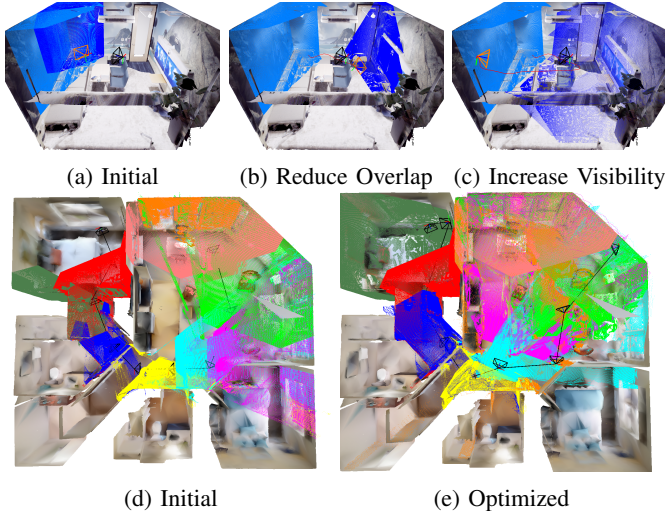


Fig. 9: Visualization of differentiable view optimization. In (a), (b) and (c), the black camera C_t is at time t . The orange camera C_{t+1} is at time $t + 1$ with optimized pose. The cyan point cloud is \mathcal{P}_t and the blue one is \mathcal{P}_{t+1} . The trajectory of C_{t+1} during the optimization process is colored in red. Starting from the setup in (a), C_{t+1} is optimized to reduce the overlap between \mathcal{P}_t and \mathcal{P}_{t+1} as shown in (b). In (c), the camera C_{t+1} gets a bigger view not overlapped with C_t 's than (b). The risk loss ensures that C_{t+1} stays away from the wall while trying to get a larger view. (d) and (e) show an example of optimizing multiple trajectory waypoints. With our method, the observed area along the trajectory is significantly larger.

D. Limitations

Our method has several limitations. The training of SDDF requires enough diversity in ray directions, which necessitates data augmentation techniques when insufficient sensor observations are available. Diversity in viewing directions is especially important for our model to excel in sparser measurements, as evident in the downsampling in our experiments. As shown in the results, our model performs worse with RGB-D measurements although the RGB-D camera generates denser observations than the LiDAR in our experiments. This is due to the RGB-D camera having a smaller vertical field of view, and hence less diversity in viewing directions. This incites a future research direction of efficiently enhancing the variety

of the viewing directions subject to a limited sensing budget. Although our method is not very sensitive to the number of ellipsoids, algorithmic addition and pruning of ellipsoids will obviate the need for choosing the correct number, and improve robustness to different scenes. The current implementation of our method is not well optimized, although it is faster than SDF-based sphere tracing. Addressing these limitations is an interesting direction for future work.

IX. CONCLUSION

In this work, we introduced a new definition of SDDF suitable for scene-level representation, and developed a model to learn such SDDFs. Our method uses ellipsoids to obtain a coarse geometric prior, and a residual network uses latent features from the ellipsoids to correct the detailed differences between the prior and the ground truth. Our experiments demonstrate that SDDF is a promising scene representation for fast novel view rendering and gradient-based viewpoint optimization. We hope that our SDDF model inspires advances in active SLAM techniques in future work.

X. ACKNOWLEDGEMENT

We gratefully acknowledge support from NSF FRR CAREER 2045945 and ARL DCIST CRA W911NF-17-2-0181.

REFERENCES

- [1] Kara-Ali Aliev, Artem Sevastopolsky, Maria Kolos, Dmitry Ulyanov, and Victor Lempitsky. Neural Point-Based Graphics. In *European Conference on Computer Vision (ECCV)*, page 696–712, 2020. 2
- [2] David Arthur and Sergei Vassilvitskii. k-means++: The Advantages of Careful Seeding. In *ACM-SIAM Symposium on Discrete Algorithms*, page 1027–1035, 2007. 7, 8, 11
- [3] Tristan Aumentado-Armstrong, Stavros Tsogkas, Sven Dickinson, and Allan Jepson. Representing 3D Shapes with Probabilistic Directed Distance Fields. In *IEEE/CVF Conference on Computer Vision and Pattern Recognition (CVPR)*, pages 19321–19332, 2022. 1, 3, 4
- [4] Jonathan T. Barron, Ben Mildenhall, Matthew Tancik, Peter Hedman, Ricardo Martin-Brualla, and Pratul P. Srinivasan. Mip-NeRF: A Multiscale Representation for Anti-Aliasing Neural Radiance Fields. In *IEEE/CVF International Conference on Computer Vision (ICCV)*, pages 5835–5844, 2021. 2
- [5] Jens Behley and C. Stachniss. Efficient Surfel-Based SLAM using 3D Laser Range Data in Urban Environments. *Robotics: Science and Systems XIV*, 2018. 1
- [6] Jen-Hao Rick Chang, Wei-Yu Chen, Anurag Ranjan, Kwang Moo Yi, and Oncel Tuzel. Pointersect: Neural Rendering with Cloud-Ray Intersection. In *IEEE/CVF Conference on Computer Vision and Pattern Recognition (CVPR)*, pages 8359–8369, 2023. 3
- [7] Angela Dai, Angel X. Chang, Manolis Savva, Maciej Halber, Thomas Funkhouser, and Matthias Nießner.

- ScanNet: Richly-annotated 3D Reconstructions of Indoor Scenes. In *IEEE/CVF Conference on Computer Vision and Pattern Recognition (CVPR)*, pages 2432–2443, 2017. [9](#), [10](#), [19](#)
- [8] Sara Fridovich-Keil, Alex Yu, Matthew Tancik, Qin-hong Chen, Benjamin Recht, and Angjoo Kanazawa. Plenoxels: Radiance Fields without Neural Networks. In *IEEE/CVF Conference on Computer Vision and Pattern Recognition (CVPR)*, pages 5491–5500, 2022. [2](#)
- [9] Stephan J. Garbin, Marek Kowalski, Matthew Johnson, Jamie Shotton, and Julien Valentin. FastNeRF: High-Fidelity Neural Rendering at 200FPS. In *IEEE/CVF International Conference on Computer Vision (ICCV)*, pages 14326–14335, 2021. [2](#)
- [10] Amos Gropp, Lior Yariv, Niv Haim, Matan Atzmon, and Yaron Lipman. Implicit Geometric Regularization for Learning Shapes. In *International Conference on Machine Learning (ICML)*, 2020. [3](#), [4](#)
- [11] John C. Hart. Sphere Tracing: a Geometric Method for the Antialiased Ray Tracing of Implicit Surfaces. *The Visual Computer*, 12:527–545, 1996. [1](#), [3](#), [9](#), [18](#), [19](#)
- [12] Peter Hedman, Pratul P. Srinivasan, Ben Mildenhall, Jonathan T. Barron, and Paul Debevec. Baking Neural Radiance Fields for Real-Time View Synthesis. In *IEEE/CVF International Conference on Computer Vision (ICCV)*, pages 5855–5864, 2021. [2](#)
- [13] Armin Hornung, Kai M. Wurm, Maren Bennewitz, Cyrill Stachniss, and Wolfram Burgard. OctoMap: An Efficient Probabilistic 3D Mapping Framework Based on Octrees. *Autonomous Robots*, 2013. [1](#)
- [14] Trevor Houchens, Cheng-You Lu, Shivam Duggal, Rao Fu, and Srinath Sridhar. NeuralODF: Learning Omnidirectional Distance Fields for 3D Shape Representation. In *arXiv preprint: arXiv 2206.05837*, 2022. [3](#)
- [15] Binbin Huang, Zehao Yu, Anpei Chen, Andreas Geiger, and Shenghua Gao. 2D Gaussian Splatting for Geometrically Accurate Radiance Fields. In *SIGGRAPH*, 2024. [2](#)
- [16] Yue Jiang, Dantong Ji, Zhizhong Han, and Matthias Zwicker. SDFDiff: Differentiable Rendering of Signed Distance Fields for 3D Shape Optimization. In *IEEE/CVF Conference on Computer Vision and Pattern Recognition (CVPR)*, pages 1248–1258, 2020. [3](#)
- [17] Sertac Karaman and Emilio Frazzoli. Sampling-based Algorithms for Optimal Motion Planning. In *arXiv preprint: arXiv 1105.1186*, 2011. [9](#)
- [18] Bernhard Kerbl, Georgios Kopanas, Thomas Leimkühler, and George Drettakis. 3D Gaussian Splatting for Real-Time Radiance Field Rendering. *ACM Transactions on Graphics*, 42(4), July 2023. [1](#), [2](#)
- [19] Borham Lee, Clark Zhang, Zonghao Huang, and Daniel D. Lee. Online Continuous Mapping using Gaussian Process Implicit Surfaces. In *IEEE International Conference on Robotics and Automation (ICRA)*, pages 6884–6890, 2019. [3](#)
- [20] Ki Myung Brian Lee, Zhirui Dai, Cedric Le Gentil, Lan Wu, Nikolay Atanasov, and Teresa Vidal-Calleja. Safe Bubble Cover for Motion Planning on Distance Fields. In *arXiv preprint: arXiv 2408.13377*, 2024. [3](#)
- [21] Shaohui Liu, Yinda Zhang, Songyou Peng, Boxin Shi, Marc Pollefeys, and Zhaopeng Cui. DIST: Rendering Deep Implicit Signed Distance Function With Differentiable Sphere Tracing. In *IEEE/CVF Conference on Computer Vision and Pattern Recognition (CVPR)*, pages 2016–2025, 2020. [3](#)
- [22] Zhuoman Liu, Bo Yang, Yan Luximon, Ajay Kumar, and Jinxi Li. RayDF: Neural Ray-Surface Distance Fields with Multi-View Consistency. In *Neural Information Processing Systems (NeurIPS)*, 2023. [3](#)
- [23] Xiaoxiao Long, Cheng Lin, Lingjie Liu, Yuan Liu, Peng Wang, Christian Theobalt, Taku Komura, and Wenping Wang. NeuralUDF: Learning Unsigned Distance Fields for Multi-View Reconstruction of Surfaces with Arbitrary Topologies. In *IEEE/CVF Conference on Computer Vision and Pattern Recognition (CVPR)*, pages 20834–20843, 2023. [3](#)
- [24] Lars Mescheder, Michael Oechsle, Michael Niemeyer, Sebastian Nowozin, and Andreas Geiger. Occupancy Networks: Learning 3D Reconstruction in Function Space. In *IEEE/CVF Conference on Computer Vision and Pattern Recognition (CVPR)*, pages 4455–4465, 2019. [1](#)
- [25] Ben Mildenhall, Pratul P. Srinivasan, Matthew Tancik, Jonathan T. Barron, Ravi Ramamoorthi, and Ren Ng. NeRF: Representing Scenes as Neural Radiance Fields for View Synthesis. In *European Conference on Computer Vision (ECCV)*, 2020. [1](#), [2](#)
- [26] Thomas Müller, Alex Evans, Christoph Schied, and Alexander Keller. Instant Neural Graphics Primitives with a Multiresolution Hash Encoding. *ACM Trans. Graph.*, 41(4), 2022. [2](#), [9](#), [10](#), [11](#), [18](#), [19](#)
- [27] Matthias Nießner, Michael Zollhöfer, Shahram Izadi, and Marc Stamminger. Real-time 3D Reconstruction at Scale Using Voxel Hashing. *ACM Trans. Graph.*, 32(6), November 2013. [3](#)
- [28] Helen Oleynikova, Zachary Taylor, Marius Fehr, Roland Siegwart, and Juan Nieto. Voxblox: Incremental 3D Euclidean Signed Distance Fields for On-board MAV Planning. In *IEEE/RSJ International Conference on Intelligent Robots and Systems (IROS)*, pages 1366–1373, 2017. [1](#), [3](#)
- [29] Jeong Joon Park, Peter Florence, Julian Straub, Richard Newcombe, and Steven Lovegrove. DeepSDF: Learning Continuous Signed Distance Functions for Shape Representation. In *IEEE/CVF Conference on Computer Vision and Pattern Recognition (CVPR)*, pages 165–174, 2019. [1](#), [3](#)
- [30] Luis Pineda, Taosha Fan, Maurizio Monge, Shobha Venkataraman, Paloma Sodhi, Ricky TQ Chen, Joseph Ortiz, Daniel DeTone, Austin Wang, Stuart Anderson, Jing Dong, Brandon Amos, and Mustafa Mukadam. Theseus: A Library for Differentiable Nonlinear Optimization. *Advances in Neural Information Processing*

- Systems*, 2022. [15](#)
- [31] Ruslan Rakhimov, Andrei-Timotei Ardelean, Victor Lempitsky, and Evgeny Burnaev. NPBG++: Accelerating Neural Point-Based Graphics. In *IEEE/CVF Conference on Computer Vision and Pattern Recognition (CVPR)*, pages 15948–15958, 2022. [2](#)
- [32] Yufan Ren, Fangjinhua Wang, Tong Zhang, Marc Pollefeys, and Sabine Süsstrunk. VolRecon: Volume Rendering of Signed Ray Distance Functions for Generalizable Multi-View Reconstruction. In *IEEE/CVF Conference on Computer Vision and Pattern Recognition (CVPR)*, pages 16685–16695, 2023. [3](#)
- [33] Antoni Rosinol, Marcus Abate, Yun Chang, and Luca Carlone. Kimera: an Open-Source Library for Real-Time Metric-Semantic Localization and Mapping. In *IEEE International Conference on Robotics and Automation (ICRA)*, pages 1689–1696, 2020. [1](#)
- [34] Erik Sandström, Yue Li, Luc Van Gool, and Martin R. Oswald. Point-SLAM: Dense Neural Point Cloud-based SLAM. In *IEEE/CVF International Conference on Computer Vision (ICCV)*, pages 18387–18398, 2023. [1](#)
- [35] Malte Splietker and Sven Behnke. Directional TSDF: Modeling Surface Orientation for Coherent Meshes. In *IEEE/RSJ International Conference on Intelligent Robots and Systems (IROS)*, pages 1727–1734, 2019. [3](#)
- [36] Julian Straub, Thomas Whelan, Lingni Ma, Yufan Chen, Erik Wijmans, Simon Green, Jakob J. Engel, Raul Mur-Artal, Carl Ren, Shobhit Verma, Anton Clarkson, Mingfei Yan, Brian Budge, Yajie Yan, Xiaqing Pan, June Yon, Yuyang Zou, Kimberly Leon, Nigel Carter, Jesus Briales, Tyler Gillingham, Elias Mueggler, Luis Pesqueira, Manolis Savva, Dhruv Batra, Hauke M. Strasdat, Renzo De Nardi, Michael Goesele, Steven Lovegrove, and Richard Newcombe. The Replica Dataset: A Digital Replica of Indoor Spaces. In *arXiv preprint: arXiv 1906.05797*, 2019. [9](#), [10](#)
- [37] Matthew Tancik, Pratul P. Srinivasan, Ben Mildenhall, Sara Fridovich-Keil, Nithin Raghavan, Utkarsh Singhal, Ravi Ramamoorthi, Jonathan T. Barron, and Ren Ng. Fourier Features Let Networks Learn High Frequency Functions in Low Dimensional Domains. In *Neural Information Processing Systems (NeurIPS)*, 2020. [11](#)
- [38] Matthew Tancik, Ethan Weber, Evonne Ng, Ruilong Li, Brent Yi, Justin Kerr, Terrance Wang, Alexander Kristoffersen, Jake Austin, Kamyar Salahi, Abhik Ahuja, David McAllister, and Angjoo Kanazawa. Nerfstudio: A Modular Framework for Neural Radiance Field Development. In *SIGGRAPH*, 2023. [2](#), [9](#), [10](#), [11](#), [16](#), [18](#), [19](#)
- [39] Peng Wang, Lingjie Liu, Yuan Liu, Christian Theobalt, Taku Komura, and Wenping Wang. NeuS: Learning Neural Implicit Surfaces by Volume Rendering for Multi-View Reconstruction. In *International Conference on Neural Information Processing Systems (NeurIPS)*, pages 27171–27183, 2021. [3](#)
- [40] Lan Wu, Ki Myung Brian Lee, Liyang Liu, and Teresa Vidal-Calleja. Faithful Euclidean Distance Field From Log-Gaussian Process Implicit Surfaces. *IEEE Robotics and Automation Letters (RA-L)*, 6(2):2461–2468, 2021. [3](#), [4](#)
- [41] Lan Wu, Ki Myung Brian Lee, Cedric Le Gentil, and Teresa Vidal-Calleja. Log-GPIS-MOP: A Unified Representation for Mapping, Odometry, and Planning. *IEEE Transactions on Robotics*, 39(5):4078–4094, 2023. [3](#)
- [42] Fei Xia, Amir R. Zamir, Zhiyang He, Alexander Sax, Jitendra Malik, and Silvio Savarese. Gibson Env: Real-World Perception for Embodied Agents. In *IEEE/CVF Conference on Computer Vision and Pattern Recognition (CVPR)*, pages 9068–9079, 2018. [9](#)
- [43] Qiangeng Xu, Zexiang Xu, Julien Philip, Sai Bi, Zhixin Shu, Kalyan Sunkavalli, and Ulrich Neumann. Point-NeRF: Point-based Neural Radiance Fields. In *IEEE/CVF Conference on Computer Vision and Pattern Recognition (CVPR)*, pages 5428–5438, 2022. [2](#)
- [44] Tarun Yenamandra, Ayush Tewari, Nan Yang, Florian Bernard, Christian Theobalt, and Daniel Cremers. FIRE: Fast Inverse Rendering using Directional and Signed Distance Functions. In *IEEE/CVF Winter Conference on Applications of Computer Vision (WACV)*, pages 3065–3075, 2024. [3](#)
- [45] Alex Yu, Ruilong Li, Matthew Tancik, Hao Li, Ren Ng, and Angjoo Kanazawa. PlenOctrees for Real-time Rendering of Neural Radiance Fields. In *IEEE/CVF International Conference on Computer Vision (ICCV)*, pages 5732–5741, 2021. [2](#)
- [46] Baowen Zhang, Chuan Fang, Rakesh Shrestha, Yixun Liang, Xiaoxiao Long, and Ping Tan. RaDe-GS: Rasterizing Depth in Gaussian Splatting. In *arXiv preprint: arXiv 2406.01467*, 2024. [2](#), [3](#), [9](#), [10](#), [11](#), [16](#), [18](#), [19](#)
- [47] Kai Zhang, Gernot Riegler, Noah Snavely, and Vladlen Koltun. NeRF++: Analyzing and Improving Neural Radiance Fields. In *arXiv preprint: arXiv 2010.07492*, 2020. [2](#)
- [48] Qian Zhang, Seung-Hwan Baek, Szymon Rusinkiewicz, and Felix Heide. Differentiable Point-Based Radiance Fields for Efficient View Synthesis. *SIGGRAPH Asia*, 2022. [2](#)
- [49] Pierre Zins, Yuanlu Xu, Edmond Boyer, Stefanie Wuhrer, and Tony Tung. Multi-View Reconstruction Using Signed Ray Distance Functions (SRDF). In *IEEE/CVF Conference on Computer Vision and Pattern Recognition (CVPR)*, pages 16696–16706, 2023. [3](#)
- [50] Ehsan Zobeidi and Nikolay Atanasov. A Deep Signed Directional Distance Function for Shape Representation. In *IEEE/RSJ International Conference on Intelligent Robots and Systems (IROS)*, pages 2689–2695, 2024. [1](#), [3](#), [4](#)
- [51] Matt Zucker, Nathan Ratliff, Anca D. Dragan, Mihail Pivtoraiko, Matthew Klingensmith, Christopher M. Dellin, J. Andrew Bagnell, and Siddhartha S. Srinivasa. CHOMP: Covariant Hamiltonian Optimization for Motion Planning. *The International Journal of Robotics Research*, 32(9-10):1164–1193, 2013. [3](#)

APPENDIX A
ELLIPSOID-BASED PRIOR NETWORK

A. Proof of Proposition 2

The intersection between the ray (\mathbf{p}, \mathbf{v}) and the ellipsoid \mathcal{E} gives the following equations:

$$\mathbf{q} = \mathbf{R}^\top (\mathbf{p} + f(\mathbf{p}, \mathbf{v}; \mathcal{E})\mathbf{v} - \mathbf{c}), \quad (31)$$

$$0 = \mathbf{q}^\top \mathbf{Q}_1^2 \mathbf{q} - \det \mathbf{Q}_0^2, \quad (32)$$

where \mathbf{q} is the intersection point expressed in coordinates in the local ellipsoid frame. Plugging (31) into (32) leads to the following quadratic equation:

$$\frac{\mathbf{v}'^\top \mathbf{Q}_1^2 \mathbf{v}'}{2} f^2 + \mathbf{p}'^\top \mathbf{Q}_1^2 \mathbf{v}' f + \frac{\mathbf{p}'^\top \mathbf{Q}_1^2 \mathbf{p}' - \det \mathbf{Q}_0^2}{2} = 0. \quad (33)$$

Solving the above equation for f , we get two roots:

$$f_{1,2} = -\frac{\sqrt{\alpha} \pm \mathbf{p}'^\top \mathbf{Q}_1^2 \mathbf{v}'}{\mathbf{v}'^\top \mathbf{Q}_1^2 \mathbf{v}'} \quad (34)$$

where α is related to the intersection indicator $i(\mathbf{p}, \mathbf{v})$ in (8):

$$\begin{aligned} \alpha &= (\mathbf{p}'^\top \mathbf{Q}_1^2 \mathbf{v}')^2 - \mathbf{v}'^\top \mathbf{Q}_1^2 \mathbf{v}' (\mathbf{p}'^\top \mathbf{Q}_1^2 \mathbf{p}' - \det \mathbf{Q}_0^2) \\ &= \mathbf{p}'^\top \mathbf{Q}_1^2 (\mathbf{v}' \mathbf{p}'^\top - \mathbf{p}' \mathbf{v}'^\top) \mathbf{Q}_1^2 \mathbf{v}' + \mathbf{v}'^\top \mathbf{Q}_1^2 \mathbf{v}' \det \mathbf{Q}_0^2 \\ &= \mathbf{p}'^\top \mathbf{Q}_1^2 \mathbf{w}'^\wedge \mathbf{Q}_1^2 \mathbf{v}' + \mathbf{v}'^\top \mathbf{Q}_1^2 \mathbf{v}' \det \mathbf{Q}_0^2 \\ &= (\mathbf{p}'^\top (\mathbf{Q}_0^2 \mathbf{w}')^\wedge \mathbf{v}' + \mathbf{v}'^\top \mathbf{Q}_1^2 \mathbf{v}') \det \mathbf{Q}_0^2 \\ &= (\mathbf{v}'^\top \mathbf{Q}_1^2 \mathbf{v}' - \mathbf{w}'^\top \mathbf{Q}_0^2 \mathbf{w}') \det \mathbf{Q}_0^2 = i(\mathbf{p}, \mathbf{v}) \det \mathbf{Q}_0^2. \end{aligned}$$

According to the SDDF definition in (2), we keep f_1 as the solution, which is exactly (7).

B. Backward Propagation

To train the prior network efficiently, we derive and implement the backward propagation of computation in Sec. IV-A and Sec. IV-B explicitly in Python instead of relying on the computation graph of PyTorch. Without loss of generality, we compute the backward propagation in the ellipsoid local frame. To efficiently compute the gradients, let $t_0 = \mathbf{v}'^\top \mathbf{Q}_1^2 \mathbf{v}'$, $t_1 = \mathbf{w}'^\top \mathbf{Q}_0^2 \mathbf{w}'$, $t_2 = \mathbf{p}'^\top \mathbf{Q}_1^2 \mathbf{p}'$, then the intersection indicator becomes $i(\mathbf{p}, \mathbf{v}) = t_0 - t_1$ and the SDDF prior is $f(\mathbf{p}, \mathbf{v}) = -(\det \mathbf{Q}_0 \sqrt{\max(i, 0) + \epsilon} + t_2)/t_0$. Given the loss \mathcal{L}_P presented in Sec. VI-C, we derive the gradients $\nabla_{\mathbf{p}'} \mathcal{L}_P$, $\nabla_{\mathbf{v}'} \mathcal{L}_P$ and $\nabla_{\mathbf{r}} \mathcal{L}_P$ via the chain rule of derivatives:

$$\nabla_{\mathbf{p}'} \mathcal{L}_P = \frac{\partial \mathcal{L}_P}{\partial i} \nabla_{\mathbf{p}'} i + \frac{\partial \mathcal{L}_P}{\partial f} \nabla_{\mathbf{p}'} f + \frac{\partial \mathcal{L}_P}{\partial s} \nabla_{\mathbf{p}'} s, \quad (35)$$

$$\nabla_{\mathbf{v}'} \mathcal{L}_P = \frac{\partial \mathcal{L}_P}{\partial i} \nabla_{\mathbf{v}'} i + \frac{\partial \mathcal{L}_P}{\partial f} \nabla_{\mathbf{v}'} f + \frac{\partial \mathcal{L}_P}{\partial s} \nabla_{\mathbf{v}'} s, \quad (36)$$

$$\nabla_{\mathbf{r}} \mathcal{L}_P = \frac{\partial \mathcal{L}_P}{\partial i} \nabla_{\mathbf{r}} i + \frac{\partial \mathcal{L}_P}{\partial f} \nabla_{\mathbf{r}} f + \frac{\partial \mathcal{L}_P}{\partial s} \nabla_{\mathbf{r}} s, \quad (37)$$

$$\nabla_{\mathbf{r}} f = \frac{\partial f}{\partial i} \nabla_{\mathbf{r}} i + \frac{\partial f}{\partial t_0} \nabla_{\mathbf{r}} t_0 + \frac{\partial f}{\partial t_2} \nabla_{\mathbf{r}} t_2 + \frac{\partial f}{\partial \mathbf{r}^\top}, \quad (38)$$

$$\nabla_{\mathbf{p}'} f = \frac{\partial f}{\partial i} \nabla_{\mathbf{p}'} i + \frac{\partial f}{\partial t_0} \nabla_{\mathbf{p}'} t_0 + \frac{\partial f}{\partial t_2} \nabla_{\mathbf{p}'} t_2, \quad (39)$$

$$\nabla_{\mathbf{v}'} f = \frac{\partial f}{\partial i} \nabla_{\mathbf{v}'} i + \frac{\partial f}{\partial t_0} \nabla_{\mathbf{v}'} t_0 + \frac{\partial f}{\partial t_2} \nabla_{\mathbf{v}'} t_2. \quad (40)$$

TABLE IV: Gradients used in backward propagation of G , \otimes denotes element-wise multiplication, and $\mathbf{U} = \mathbf{r}^\wedge \otimes \mathbf{r}^\wedge$.

	$\nabla_{\mathbf{p}'}$	$\nabla_{\mathbf{v}'}$	$\nabla_{\mathbf{r}}$
t_0	$\mathbf{0}$	$2\mathbf{Q}_1^2 \mathbf{v}'$	$2\mathbf{Q}_0 \mathbf{U}(\mathbf{v}' \otimes \mathbf{v}')$
t_1	$2\mathbf{v}' \times \mathbf{Q}_0^2 \mathbf{w}'$	$-2\mathbf{p}' \times \mathbf{Q}_0^2 \mathbf{w}'$	$2(\text{diag}(\mathbf{w}'))^2 \mathbf{r}$
t_2	$\mathbf{Q}_1^2 \mathbf{v}'$	$\mathbf{Q}_1^2 \mathbf{p}'$	$2\mathbf{Q}_0 \mathbf{U}(\mathbf{p}' \otimes \mathbf{v}')$
i	$\nabla_{\mathbf{p}'} t_0 - \nabla_{\mathbf{p}'} t_1$	$\nabla_{\mathbf{v}'} t_0 - \nabla_{\mathbf{v}'} t_1$	$\nabla_{\mathbf{r}} t_0 - \nabla_{\mathbf{r}} t_1$
s	$2\mathbf{Q}_1^2 \mathbf{p}'$	$\mathbf{0}$	$2\mathbf{Q}_0 (\mathbf{U}(\mathbf{p}' \otimes \mathbf{p}') - \mathbf{Q}_1^2 \mathbf{1})$

TABLE V: Partial derivatives used in backward propagation of G . When $t_0 \approx 0$, which is a degraded configuration, $\frac{\partial f}{\partial i}$, $\frac{\partial f}{\partial t_0}$ and $\frac{\partial f}{\partial t_2}$ are set to 0.

	$\frac{\partial}{\partial i}$	$\frac{\partial}{\partial t_0}$	$\frac{\partial}{\partial t_2}$	$\frac{\partial}{\partial \mathbf{r}^\top}$
f	$-\frac{\det \mathbf{Q}_0}{2t_0 \sqrt{i+\epsilon}}$	$-\frac{f}{t_0}$	$-\frac{1}{t_0}$	$-\frac{\sqrt{\max(i, 0) + \epsilon}}{t_0} \mathbf{Q}_1 \mathbf{1}$

And the related intermediate results are shown in Table. IV and Table. V.

To compute the gradients $\nabla_{\mathbf{p}} \mathcal{L}_P$, $\nabla_{\mathbf{v}} \mathcal{L}_P$, $\nabla_{\mathbf{R}} \mathcal{L}_P$, and $\nabla_{\mathbf{c}} \mathcal{L}_P$, we can apply the chain rule of derivatives again. Since

$$\mathbf{p}' = \mathbf{R}^\top (\mathbf{p} - \mathbf{c}), \quad (41)$$

$$\mathbf{v}' = \mathbf{R}^\top \mathbf{v}, \quad (42)$$

we can get

$$\nabla_{\mathbf{p}} \mathcal{L}_P = \mathbf{R} \nabla_{\mathbf{p}'} \mathcal{L}_P, \quad (43)$$

$$\nabla_{\mathbf{v}} \mathcal{L}_P = \mathbf{R} \nabla_{\mathbf{v}'} \mathcal{L}_P, \quad (44)$$

$$\nabla_{\mathbf{R}} \mathcal{L}_P = (\mathbf{p} - \mathbf{c}) \nabla_{\mathbf{p}'}^\top \mathcal{L}_P, \quad (45)$$

$$\nabla_{\mathbf{c}} \mathcal{L}_P = -\mathbf{R} \nabla_{\mathbf{p}'} \mathcal{L}_P, \quad (46)$$

which can be computed by the computation graph of PyTorch with little effort. However, a custom implementation may save the GPU memory and compute the results faster.

Then, to compute the gradients with respect to the pose parameters $\xi = (\rho, \theta) \in \mathbb{R}^6$, we refer to Theseus [30], which provides an efficient implementation of gradient computation for Lie algebra. For convenience and readers' interest, we present the result of $\mathbf{T} = \mathbf{T}_0 \exp(\xi^\wedge)$ (for simplicity, we assume $\mathbf{T}_0 = \mathbf{I}$ here.) and gradient $\nabla_{\xi} \mathcal{L}_P$ here:

$$\mathbf{T} = \begin{bmatrix} \mathbf{R} & \mathbf{t} \\ \mathbf{0}^\top & 1 \end{bmatrix} = \exp(\hat{\xi}) = \begin{bmatrix} \exp(\hat{\theta}) & J_R(\theta)^\top \rho \\ \mathbf{0} & 1 \end{bmatrix}, \quad (47)$$

$$\mathbf{R} = \exp(\hat{\theta}) = \mathbf{I} + \frac{\sin \|\theta\|}{\|\theta\|} \hat{\theta} + \frac{1 - \cos \|\theta\|}{\|\theta\|^2} \hat{\theta}^2, \quad (48)$$

$$J_R(\theta) = \mathbf{I} - \frac{1 - \cos \|\theta\|}{\|\theta\|^2} \hat{\theta} + \frac{\|\theta\| - \sin \|\theta\|}{\|\theta\|^3} \hat{\theta}^2, \quad (49)$$

$$\nabla_{\xi} \mathcal{L}_P = J_R(\xi)^\top \begin{bmatrix} \mathbf{R}^\top \nabla_{\mathbf{c}} \mathcal{L}_P \\ \mathbf{W}_{32} - \mathbf{W}_{23} \\ \mathbf{W}_{13} - \mathbf{W}_{31} \\ \mathbf{W}_{21} - \mathbf{W}_{12} \end{bmatrix}, \quad (50)$$

where

$$\mathbf{W} = \mathbf{R}^\top \nabla_{\mathbf{R}} \mathcal{L}_P, \quad (51)$$

$$\mathcal{J}_R(\boldsymbol{\xi}) = \begin{bmatrix} J_R(\boldsymbol{\theta}) & Q_R(\boldsymbol{\xi}) \\ \mathbf{0}_{3 \times 3} & J_R(\boldsymbol{\theta}) \end{bmatrix}, \quad (52)$$

$$Q_R(\boldsymbol{\xi}) = \mathbf{R}^\top \mathbf{L}. \quad (53)$$

And

$$\begin{aligned} \mathbf{L} = \mathbf{R} Q_R(\boldsymbol{\xi}) &= \frac{\cos \|\boldsymbol{\theta}\| - 1}{\|\boldsymbol{\theta}\|^2} \hat{\boldsymbol{\rho}} \\ &- \frac{\|\boldsymbol{\theta}\| - \sin \|\boldsymbol{\theta}\|}{\|\boldsymbol{\theta}\|^3} \left((\boldsymbol{\theta} \times \boldsymbol{\rho})^\wedge + \boldsymbol{\rho} \boldsymbol{\theta}^\top - \boldsymbol{\theta}^\top \boldsymbol{\rho} \mathbf{I} \right) \\ &+ \left(\frac{\sin \|\boldsymbol{\theta}\|}{\|\boldsymbol{\theta}\|^3} + \frac{2(\cos \|\boldsymbol{\theta}\| - 1)}{\|\boldsymbol{\theta}\|^4} \right) (\boldsymbol{\theta} \times \boldsymbol{\rho}) \boldsymbol{\theta}^\top \\ &- \left(\frac{\cos \|\boldsymbol{\theta}\| - 1}{\|\boldsymbol{\theta}\|^4} + \frac{3(\|\boldsymbol{\theta}\| - \sin \|\boldsymbol{\theta}\|)}{\|\boldsymbol{\theta}\|^5} \right) \left(\boldsymbol{\theta} \times (\boldsymbol{\theta} \times \boldsymbol{\rho}) \boldsymbol{\theta}^\top \right), \end{aligned} \quad (54)$$

where many intermediate results from computing \mathbf{R} and $J_R(\boldsymbol{\theta})$ can be reused. In our experiments, we find that this custom implementation of gradient computation is essential for using the GPU efficiently. Otherwise, the PyTorch computation graph will take too much GPU memory and compute the gradients slowly. Currently, this backward propagation is implemented in Python, which could be accelerated dramatically by a CUDA alternative.

C. Proof of Proposition 3

Without loss of generality, we can prove Proposition 3 in the local frame of the selected ellipsoid. According to Table. IV and Table. V in Sec. A-B, we have

$$\mathbf{v}'^\top \nabla_{\mathbf{p}'} t_0 = 0, \quad (55)$$

$$\mathbf{v}'^\top \nabla_{\mathbf{p}'} t_1 = 0, \quad (56)$$

$$\mathbf{v}'^\top \nabla_{\mathbf{p}'} t_2 = t_0. \quad (57)$$

So, we get:

$$\mathbf{v}'^\top \nabla_{\mathbf{p}'} f + 1 = 0, \quad (58)$$

which is the directional Eikonal equation for SDDF.

APPENDIX B RESIDUAL NETWORK

A. Proof of Proposition 4

The SDDF $\hat{f}(\mathbf{p}, \mathbf{v})$ in (23) computed by the combination of the prior and the residual networks satisfies the SDDF directional Eikonal equation in (4).

Since the ellipsoid prior network P satisfies (4) according to Proposition 3, we have $\mathbf{v}'^\top \nabla_{\mathbf{p}'} f = -1$. Then, because

$$\begin{aligned} \mathbf{v}'^\top \nabla_{\mathbf{p}'} \delta_f &= \mathbf{v}'^\top \nabla_{\mathbf{p}'} \mathbf{q} \nabla_{\mathbf{q}} \delta_f \\ &= \mathbf{v}'^\top \left(\mathbf{I} + \nabla_{\mathbf{p}'} f \mathbf{v}'^\top \right) \nabla_{\mathbf{q}} \delta_f \\ &= \mathbf{0}^\top \nabla_{\mathbf{q}} \delta_f = 0, \end{aligned} \quad (59)$$

we get $\mathbf{v}'^\top \nabla_{\mathbf{p}'} \hat{f} = \mathbf{v}'^\top \nabla_{\mathbf{p}'} f + \mathbf{v}'^\top \nabla_{\mathbf{p}'} \delta_f = -1$.

APPENDIX C TRAINING DETAILS

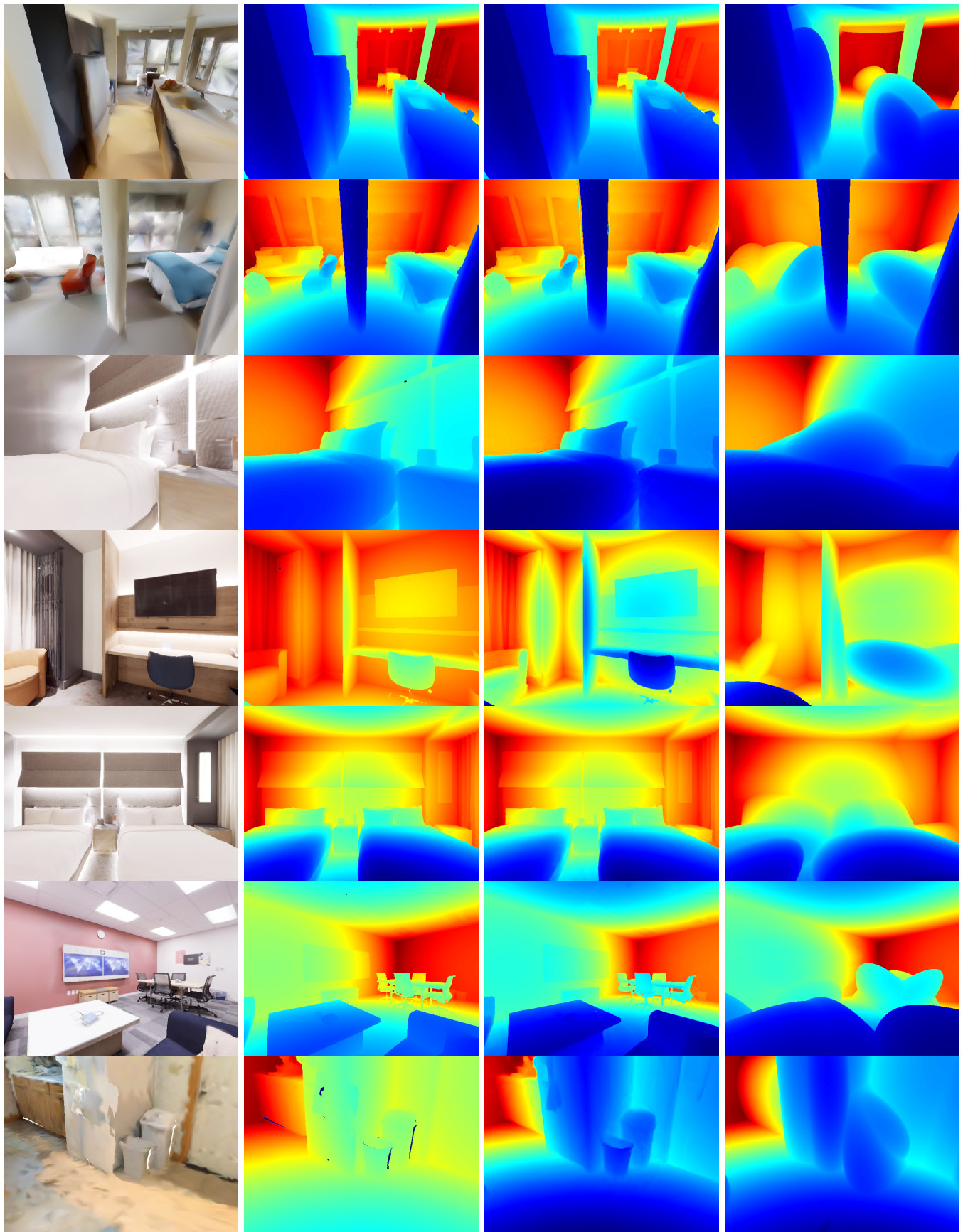
We use 256 ellipsoids for the Allensville scene and 128 for other scenes. The dimension of the latent feature is $m = 256$. The decoder is a 7-layer MLP of dimensions [256, 256, 512, 512, 256, 128, 64] with skip connections at the first and third layers. LeakyReLU is used as the nonlinear layer.

Our model is optimized by Adam with a learning rate 0.001 for the first 150 epochs and 0.0001 for another 150 epochs. Each batch for training has 512k rays. The prior network is pretrained for 19k batch iterations and then trained together with the residual network for another 1k batch iterations. Then, the prior network is frozen, and we optimize the residual network only for the remaining epochs.

The SDF model is trained with a batch size of 60, Adam optimizer, and a learning rate 0.0001 for 300 epochs. RaDeGS [46] is trained for 30k iterations with default settings. Nerfacto [38] is trained for 50k iterations without camera pose optimization because the ground truth camera pose is provided.

APPENDIX D MORE VISUALIZATION

We present more visualizations of SDDF prediction by our method for different scenes in Fig. 10. In Figs. 11 and 12, more examples are shown to compare our method and the baselines.



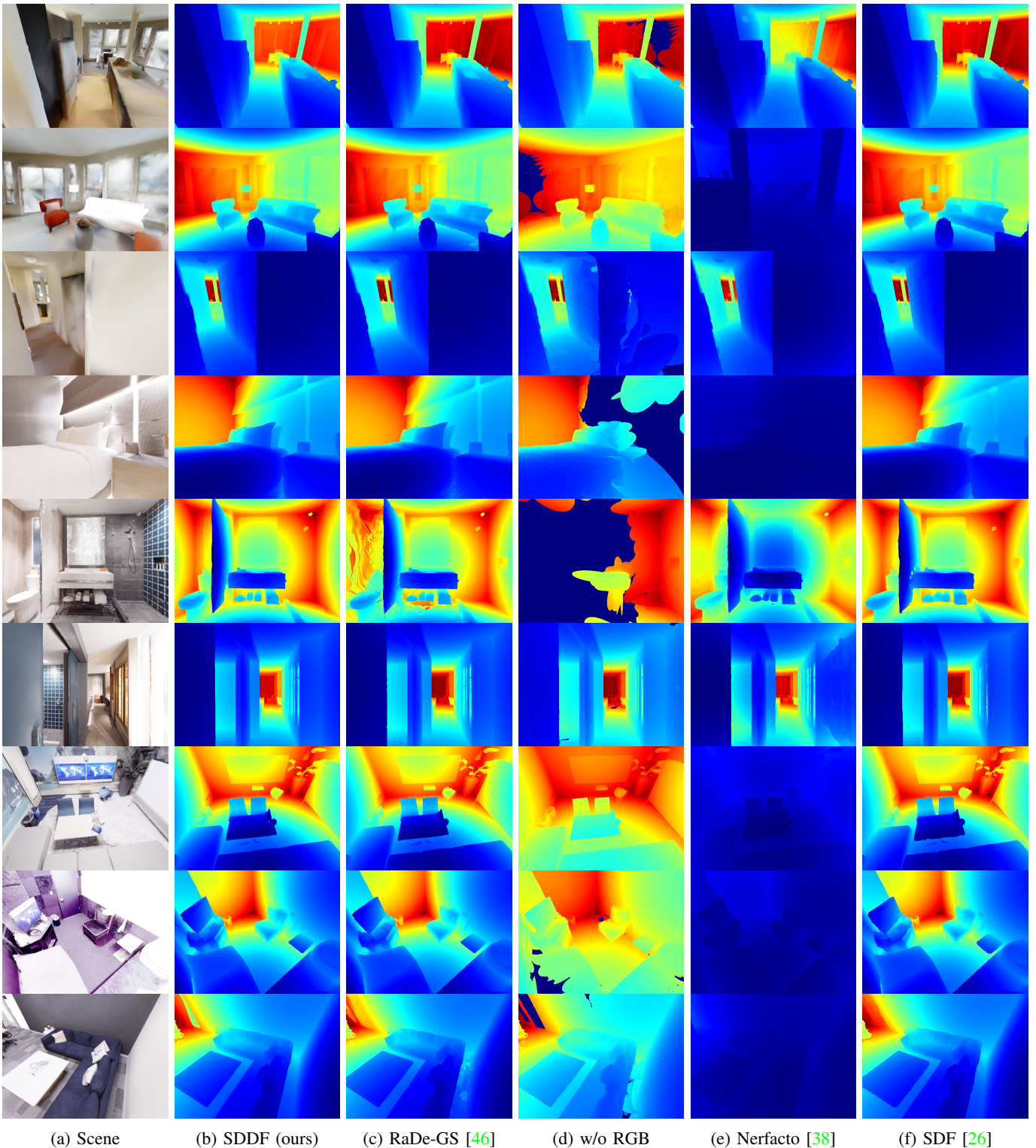
(a) Scene

(b) SDDF Ground Truth

(c) SDDF Prediction

(d) SDDF Prior

Fig. 10: More qualitative results of our method. The four columns are the RGB images of the view, the ground truth SDDF (color scale may be different due to the occasional zeros caused by mesh holes), the SDDF prediction by our method, and the SDDF prior generated by the ellipsoid-based prior network in our SDDF model.



(a) Scene (b) SDDF (ours) (c) RaDe-GS [46] (d) w/o RGB (e) Nerfacto [38] (f) SDF [26]

Fig. 11: More qualitative SDDF prediction comparison between our method and baselines on synthesized datasets, Replica and Gibson. The six columns are the RGB images of the scene, SDDF prediction by our method, RaDe-GS [46], RaDe-GS [46] trained without RGB images, Nerfacto [38] and SDF-Instant-NGP [26] with sphere tracing [11] respectively. When only a few sensor measurements are available, RaDe-GS [46] fails to learn the geometry, giving splatting artifacts. When trained without RGB, RaDe-GS presents instability in certain cases shown above. The splatting artifacts are more significant. And even worse, it cannot learn the scene when available measurements becomes fewer. Nerfacto produces cloud like artifacts when no sufficient data is provided such as the sixth row. And it has large distance errors in some cases like the second row. Some pixels have much larger distance values. Thus, the image looks blue globally. SDF-Instant-NGP [26] tends to learn smoother shapes that lack sharper details, like the fourth row. And the accumulated errors by sphere tracing may cause holes on objects or rough object boundaries. e.g., the curtain in the figure of the fifth row and the closet in the figure of the sixth row.

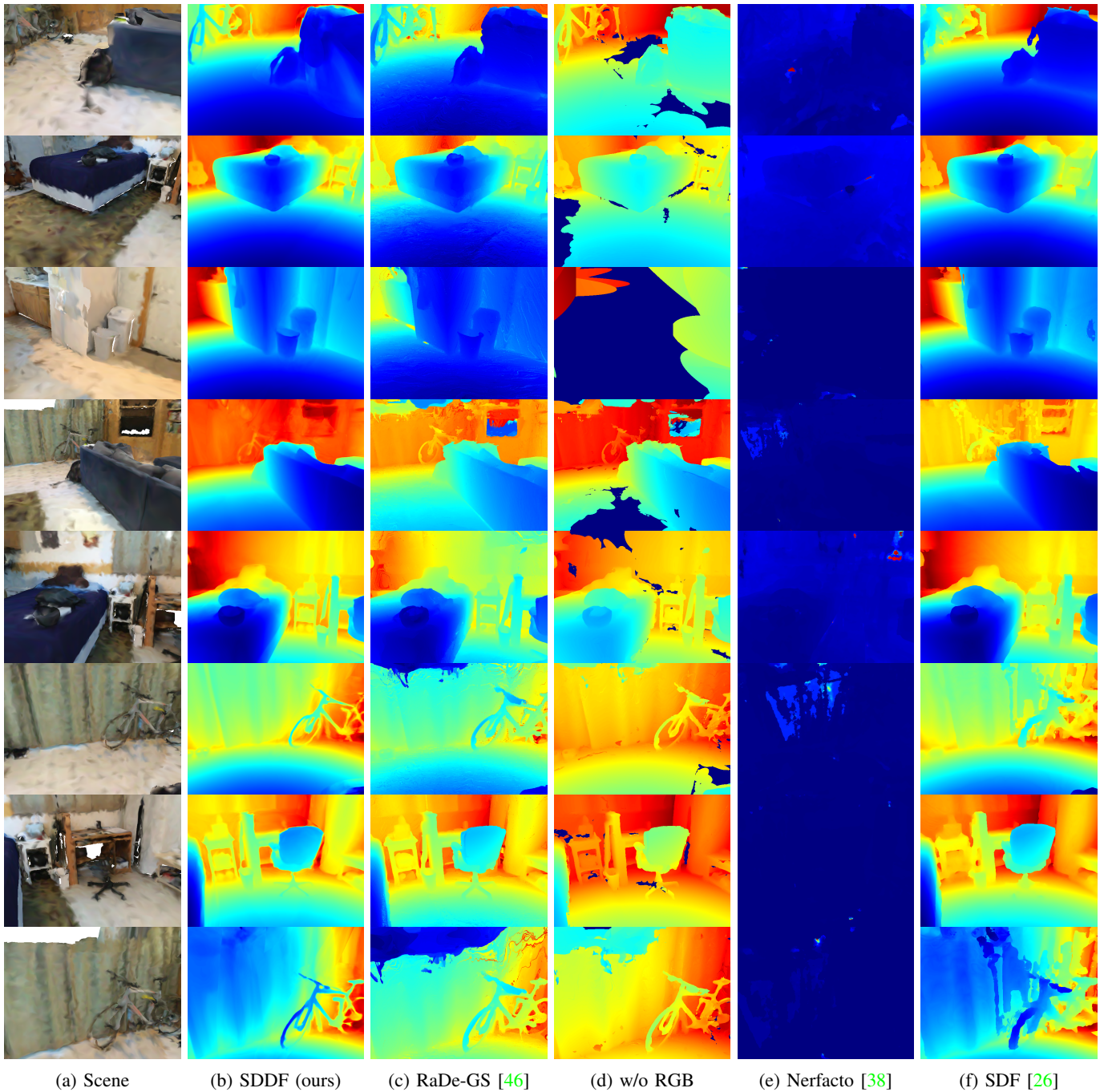


Fig. 12: More qualitative SDDF prediction comparison between our method and baselines on real data from ScanNet [7] scene 0000-00. The six columns are the RGB images of the scene, SDDF prediction by our method, RaDe-GS [46], RaDe-GS [46] trained without RGB images, Nerfacto [38] and SDF-Instant-NGP [26] with sphere tracing [11]. The results lead to the same conclusion we draw from the synthesized datasets.